Substrate-Gated Transformation of a Pre-Catalyst into an Iron-Hydride Intermediate $[(NO)_2(CO)Fe(\mu\text{-}H)Fe(CO)(NO)_2]^-$ for Catalytic Dehydrogenation of Dimethylamine Borane

Yu-Ting Tseng,[1,2] Vladimir Pelmenschikov,*[3] Linda Iffland-Mühlhaus,[4] Donato Calabrese,[5] Yu-Che Chang,[2] Konstantin Laun,[3] Chih-Wen Pao,[6] Ilya Sergueev,[7] Yoshitaka Yoda,[8] Wen-Feng Liaw,[1] Chien-Hong Chen,*[9] I-Jui Hsu,*[10] Ulf-Peter Apfel,*[4,11] Giorgio Caserta,*[3] Lars Lauterbach,*[5] and Tsai-Te Lu*[1,2]

Affiliations:

[1]Department of Chemistry, National Tsing Hua University, Hsinchu 30013, Taiwan.

[2]Institute of Biomedical Engineering, National Tsing Hua University, Hsinchu 30013, Taiwan.

[3]Institut für Chemie, Technische Universität Berlin, 10623 Berlin, Germany.

[4]Department of Chemistry and Biochemistry, Inorganic Chemistry I, Ruhr-Universität Bochum, 44801, Bochum, Germany.

[5]Institute of Applied Microbiology, RWTH Aachen University, Aachen, Germany.

[6]National Synchrotron Radiation Research Center, Hsinchu 30076, Taiwan.

[7]Deutsches Elektronen-Synchrotron DESY, D-22607 Hamburg, Germany.

[8]JASRI, SPring-8, Sayo-gun, Hyogo 679-5198, Japan.

[9]Department of Medical Applied Chemistry, Chung Shan Medical University and Department of Medical Education, Chung Shan Medical University Hospital, Taichung 40201, Taiwan.

[10]Department of Molecular Science and Engineering, Research and Development Center of Smart Textile Technology, National Taipei University of Technology, Taipei 10608, Taiwan.

[11]Fraunhofer UMSICHT, Department for Electrosynthesis, 46047 Oberhausen, Germany.

***Corresponding author:**

Vladimir Pelmenschikov, Ph.D., Institut für Chemie, Technische Universität Berlin, 10623 Berlin, Germany. E-mail: pelmentschikov@tu-berlin.de.

Chien-Hong Chen, Ph.D., Department of Medical Applied Chemistry, Chung Shan Medical University and Department of Medical Education, Chung Shan Medical University Hospital, Taichung 40201, Taiwan. E-mail: cchwind@csmu.edu.tw.

I-Jui Hsu, Ph.D., Department of Molecular Science and Engineering, Research and Development Center of Smart Textile Technology, National Taipei University of Technology, Taipei 10608, Taiwan. E-mail: ijuihsu@mail.ntut.edu.tw.

Ulf-Peter Apfel, Ph.D., Department of Chemistry and Biochemistry, Inorganic Chemistry I, Ruhr-Universität Bochum, 44801, Bochum, Germany. E-mail: ulf.apfel@rub.de.

Giorgio Caserta, Ph.D., Institut für Chemie, Technische Universität Berlin, 10623 Berlin, Germany. E-mail: giorgio.caserta@tu-berlin.de.

Lars Lauterbach, Ph.D., Institute of Applied Microbiology, RWTH Aachen University, Aachen, Germany. E-mail: lars.lauterbach@rwth-aachen.de.

Tsai-Te Lu, Ph.D., Institute of Biomedical Engineering & Department of Chemistry, National Tsing Hua University, Hsinchu, 300044 Taiwan. E-mail: ttlu@mx.nthu.edu.tw.

Abstract

Continued efforts are made on the development of earth-abundant metal catalysts for dehydrogenation/hydrolysis of amine boranes. In this study, complex [K-18-crown-6-ether][$(NO)_2Fe(\mu$-$^{Me}Pyr)(\mu$-$CO)Fe(NO)_2$] (**3-K-crown**, ^{Me}Pyr = 3-methylpyrazolate) was explored as a pre-catalyst for the dehydrogenation of dimethylamine borane (DMAB). Upon evolution of $H_{2(g)}$ from DMAB triggered by **3-K-crown**, parallel conversion of **3-K-crown** into $[(NO)_2Fe(N,N'$-$^{Me}PyrBH_2NMe_2)]^-$ (**5**) and an iron-hydride intermediate $[(NO)_2(CO)Fe(\mu$-$H)Fe(CO)(NO)_2]^-$ (**A**) was evidenced by XRD/NMR/IR/nuclear resonance vibrational spectroscopy (NRVS) experiments and supported by DFT calculations. Subsequent transformation of **A** into complex $[(NO)_2Fe(\mu$-$CO)_2Fe(NO)_2]^-$ (**6**) is synchronized with the deactivated generation of $H_{2(g)}$. Through reaction of complex [Na-18-crown-6-ether][$(NO)_2Fe(\eta^2$-$BH_4)$] (**4-Na-crown**) with $CO_{(g)}$ as an alternative synthetic route, moreover, isolated intermediate [Na-18-crown-6-ether][$(NO)_2(CO)Fe(\mu$-$H)Fe(CO)(NO)_2$] (**A-Na-crown**) featuring catalytic reactivity toward dehydrogenation of DMAB supports a substrate-gated transformation of pre-catalyst $[(NO)_2Fe(\mu$-$^{Me}Pyr)(\mu$-$CO)Fe(NO)_2]^-$ (**3**) into the iron-hydride species **A** as an intermediate during the generation of $H_{2(g)}$.

Introduction

Due to the high hydrogen content (up to 19.6 wt%) and thermal stability in air, amine boranes (R_2NHBH_3) have recently been extensively investigated for generation of $H_{2(g)}$,[1-8] while improvements on regeneration of amine boranes after the thermodynamically-driven dehydrogenation/hydrolysis reactions await continued investigations.[9-11] As a hydrogen-rich vehicle, amine boranes were also reported for transfer hydrogenation of imines, olefins, nitroarenes, aldehydes, and ketones.[12-16] In addition to $H_{2(g)}$ release and transfer, dehydrogenation of amine boranes can result in the formation of aminoborane B-N products, which are isoelectronic main group analogues of olefins for production of inorganic polyolefins/hexagonal BN and for applications as functional B-N materials.[3-8] To advance the development of (non-)noble transition metal catalysts, mechanistic studies explored the critical formation of metal-hydride intermediates during the (catalytic) dehydrogenation of amine boranes. In heterogenous transition metal nanoparticles, kinetic/spectroscopic/computational studies demonstrate that metal-mediated cleavage of B-H bond in amine boranes and activation of O-H bond in water promote the subsequent dehydrogenation of generated M-H species leading to catalytic generation of $H_{2(g)}$ via the hydrolytic mechanism.[17-19] In molecular transition metal complexes,[3-8] crystallographic investigations on amine-borane σ-complex (M = Cr, Mn, Cu, Zr, Ru, Rh, and Ir),[20-26] metal amido-borane complex (M = Mg, Ca, Sr, Sc, Ti, Co, Zr, and La),[27-33] metal boryl complex (M = Rh),[34] and hydrido amido-borane complex (M = Co, Zr) provide direct insights into the binding and activation of amine boranes by coordination-unsaturated and redox-active/Lewis acid metal centers.[31, 35-36] In particular, oxidative addition of N-H bonds (or B-H bonds) in amine boranes by low-valence metal complexes occurs before generation of metal dihydride adducts (M = Mo, Ir), whereas the subsequent elimination

of $H_{2(g)}$ completes the catalytic cycle (Scheme 1a).[3-8, 37-38] Ligand-assisted deprotonation of the N-H bond in (metal-bound) amine boranes and assembly of metal hydride species via concerted or stepwise mechanisms was also reported to facilitate the catalytic dehydrogenation of amine boranes (Scheme 1b).[3-8, 23, 29-30, 32, 39-46] In addition, nucleophilic attack of exogenous Lewis base (e.g. $NHMe_2$) onto metal-bound amine boranes provides an alternative pathway triggering the B-H bond cleavage and yielding metal-hydride species for catalytic dehydrogenation of amine boranes (Scheme 1c).[3-8, 47-48]

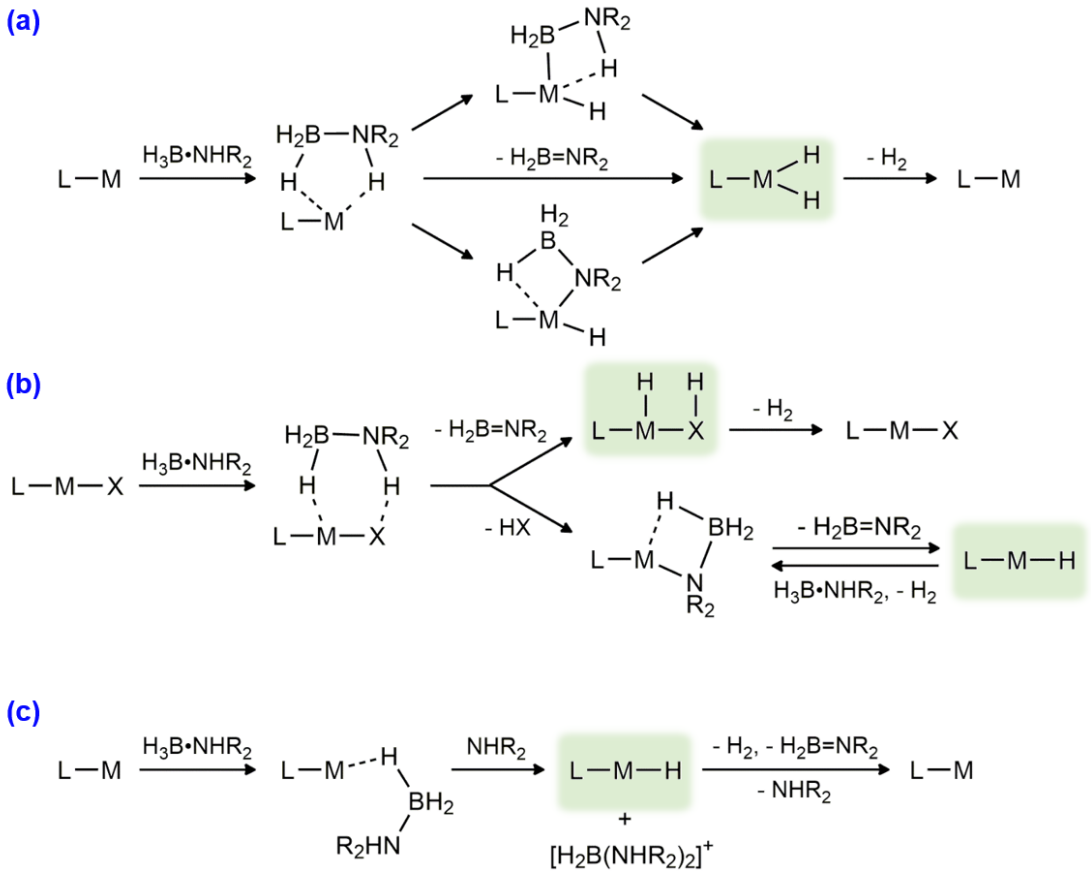

Scheme 1. (**a**-**c**) Mechanisms for catalytic dehydrogenation of amine boranes promoted by (non-)noble transition metal catalysts.

In comparison with the spontaneous dehydrogenation of amine boranes catalyzed by molecular Fe catalysts,[40-46] iron-carbonyl complexes shown in Chart 1a were

discovered as pre-catalysts requiring a photo-activation process.[49-53] Manners and co-workers pioneered in the development of complex $[(\eta^5\text{-}C_5H_5)Fe(CO)_2]_2$ for photolytic dehydrogenation of NH_3BH_3. Moreover, the photo-triggered dissociation of CO and halide from $[(\eta^5\text{-}C_5H_5)Fe(CO)_2X]$ enables the binding of Me_2NHBH_3 (DMAB) to afford transient $[(\eta^5\text{-}C_5H_5)Fe(CO)(DMAB)]$ species and promotes the catalytic generation of $H_{2(g)}$.[52] In addition, Bengali, Darensbourg and co-workers reported a reactivity, kinetic, and computational study of diiron complexes $(\mu\text{-}SCH_2XCH_2S)$-$[Fe(CO)_3]_2$ as photo-activated pre-catalysts for dehydrogenation of DMAB.[53] These bioinspired Fe-CO complexes clarified the critical role of photo-labile CO ligands on the transient formation of a coordination-unsaturated Fe center, which binds and activates amine boranes for catalytic evolution of $H_{2(g)}$.

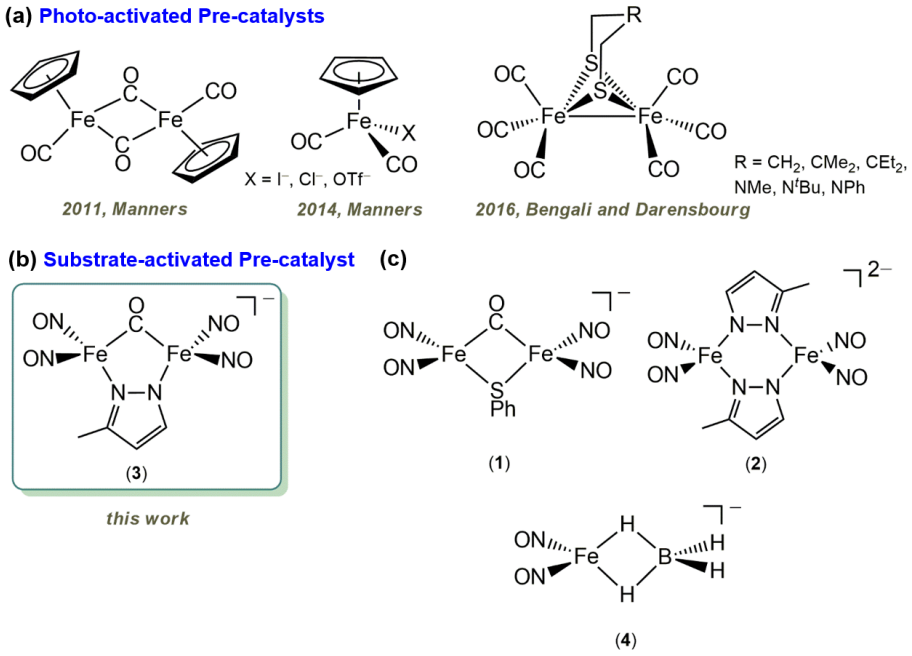

Chart 1. (**a**) Reported Fe-CO complexes as photo-activated pre-catalysts for dehydrogenation of amine boranes. (**b**) Dinitrosyl iron complex (DNIC) $[(NO)_2Fe(\mu\text{-}^{Me}Pyr)(\mu\text{-}CO)Fe(NO)_2]^-$ (**3**) as a substrate-activated pre-catalyst for dehydrogenation of Me_2NHBH_3 (DMAB). (**c**) Other DNICs explored in this study.

Recently, the redox-active $[Fe(NO)_2]$ unit in dinitrosyl iron complexes (DNICs) was explored as a translational model for the activation of small molecules (i.e. $H_2O/O_2/NO/NO_2^-/NO_3^-$ or CS_2/CO_2) and (electro)catalytic water splitting process.[54-67] During the (electro)catalytic water splitting promoted by DNICs, in particular, iron-hydride species with $\{Fe(NO)_2\}^8/\{Fe(NO)_2\}^9$ electronic structures, i.e. $[M(\mu\text{-}H)Fe(NO)_2]$ (M = Fe or Ni), $[M(\mu\text{-}H)Fe(NO)_2(H)]$, or $[(H)Fe(NO)_2]$ species, were proposed as the active intermediates for evolution of $H_{2(g)}$.[55-57] Through reaction of $\{Fe(NO)_2\}^{10}$ DNIC $[(NO)_2Fe(TMEDA)]$ with $[BH_4]^-$, hydride-containing DNIC $[(NO)_2Fe(\eta^2\text{-}BH_4)]^-$ (**4**, Chart 1c) can promote the hydride insertion into CS_2 (or CO_2) leading to the formation of Fe-bound $[HCS_2]^-$ in the form of $[(NO)_2Fe(\eta^3\text{-}HCS_2)]^-$ (or released $[HCO_2]^-$).[66] Relying on the interconversion between dinuclear and mononuclear DNICs, of importance, nucleophilic reactivity of dinuclear DNIC $[(NO)_2Fe(\mu\text{-}^{Me}Pyr)_2Fe(NO)_2]^{2-}$ (**2**, Chart 1c) was reported to bind and activate CO_2 yielding mononuclear DNIC $[(NO)_2Fe(^{Me}PyrCO_2)]^-$ ($^{Me}PyrCO_2$ = 3-methyl-pyrazole-1-carboxylate), which featured a Ca^{2+}-promoted conversion of captured CO_2 into oxalate.[67]

In this study, a diamagnetic $\{Fe(NO)_2\}^{10}$-$\{Fe(NO)_2\}^{10}$ DNIC $[(NO)_2Fe(\mu\text{-}^{Me}Pyr)(\mu\text{-}CO)Fe(NO)_2]^-$ (**3**, Chart 1b) was explored as a pre-catalyst for dehydrogenation of dimethylamine borane (DMAB). Based on the ^1H NMR, IR, nuclear resonance vibrational spectroscopy (NRVS),[68-69] single-crystal X-ray diffraction, and density functional theory (DFT) calculations, an iron-hydride species $[(NO)_2(CO)Fe(\mu\text{-}H)Fe(CO)(NO)_2]^-$ (**A**) derived from reaction of DNIC [K-18-crown-6-ether]$[(NO)_2Fe(\mu\text{-}^{Me}Pyr)(\mu\text{-}CO)Fe(NO)_2]$ (**3-K-crown**, ^{Me}Pyr = 3-methylpyrazolate) and DMAB was identified as an intermediate generated during the catalytic evolution

of $H_{2(g)}$ from DMAB. Moreover, subsequent transformation of intermediate **A** into dinuclear DNIC $[(NO)_2Fe(\mu\text{-}CO)_2Fe(NO)_2]^-$ (**6**) explains the deactivation mechanism for the catalytic process.

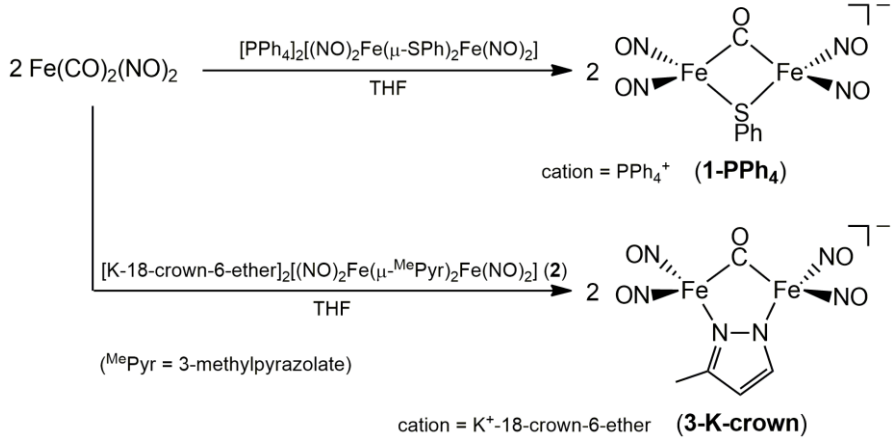

Scheme 2. Synthetic methodology for DNICs **1-PPh4** and **3-K-crown**.

Results and Discussion

Synthesis and Characterization of DNIC [K-18-crown-6-ether][$(NO)_2Fe(\mu$-^{Me}Pyr)(μ-CO)Fe$(NO)_2$] (3-K-crown). Relevant to the reported synthesis of $[PPh_4][(NO)_2Fe(\mu\text{-}SPh)(\mu\text{-}CO)Fe(NO)_2]$ (**1-PPh4**),[70] addition of two equiv. of $Fe(CO)_2(NO)_2$ into the THF solution of $[K\text{-}18\text{-}crown\text{-}6\text{-}ether]_2[(NO)_2Fe(\mu\text{-}^{Me}Pyr)_2Fe(NO)_2]$ (**2-K-crown**) at ambient temperature led to the formation of DNIC [K-18-crown-6-ether][$(NO)_2Fe(\mu$-^{Me}Pyr)(μ-CO)Fe$(NO)_2$] (**3-K-crown**, Scheme 2 and Figure 1a). As shown in Figure S1, DNIC **3-K-crown** exhibits IR ν_{NO} and ν_{CO} stretching frequencies at 1699, 1684, and 1840 cm^{-1}, respectively, which are similar to those at 1706, 1694, and 1846 cm^{-1} of DNIC **1-PPh4**.[70] In addition, $Fe_{1s}\rightarrow Fe_{3d}$ pre-edge energies at 7113.6, 7113.5, and 7113.7 eV featured by DNICs **1-PPh4**, **2-K-crown**, and **3-K-crown**, respectively, supported their $\{Fe(NO)_2\}^{10}$-$\{Fe(NO)_2\}^{10}$ electronic structures (Table 1 and Figure S2).[67, 70-71] In comparison with DNIC **2-K-crown**, a

slightly higher Fe_{1s}→Fe_{3d} pre-edge energy and down-field ^{1}H NMR signals at δ = 7.38, 6.01, and 2.18 ppm featured by DNIC **3-K-crown** revealed an Fe-to-CO backbonding interaction between the diamagnetic $\{Fe(NO)_2\}^{10}$-$\{Fe(NO)_2\}^{10}$ core and bridging CO (Figure S3).[67] Besides the ^{13}C NMR signals at 151.3, 145.6, 105.2, and 11.8 ppm derived from the bridging 3-methylpyrazolate ligand, the ^{13}C NMR signal of bridging CO in diamagnetic DNIC **3-K-crown** locates at 260.1 ppm (Figure 1c).[72-73]

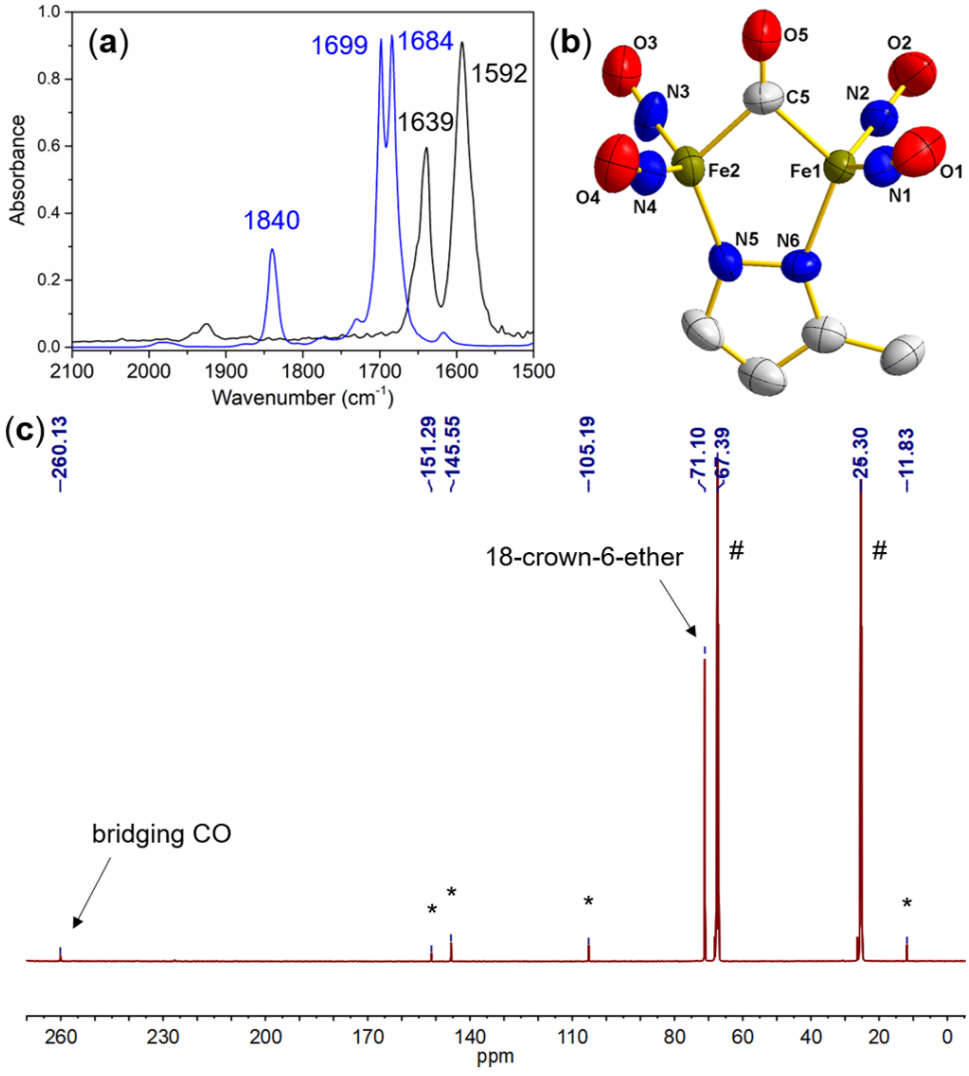

Figure 1. (**a**) IR spectrum of DNIC **3-K-crown** (blue) derived from reaction of $Fe(CO)_2(NO)_2$ and DNIC **2-K-crown** in a 2:1 stoichiometry in THF. IR spectrum of DNIC **2-K-crown** in THF is shown in black. (**b**) ORTEP drawing and labeling scheme of DNIC **3-K-crown** with thermal ellipsoids drawn at 50% probability. [K-18-crown-6-ether]$^{+}$ countercation is omitted for clarity. (**c**) ^{13}C NMR spectrum of DNIC **3-K-crown** in d_8-THF (*: 3-methylpyrazolate; #: d_8-THF).

Table 1. Apparent Fe_{1s}→Fe_{3d} Pre-edge Energies, Mössbauer Parameters,[a] IR ν_{NO}/ν_{CO} Stretching Frequencies, and Selected Bond Distances for Dinuclear DNICs **1-PPh4**, **2-K-crown**, **3-K-crown**, **4-K-crown**, **A-Na-cryptand**, and $[(NO)_2Fe(\mu\text{-}SPh)_2Fe(NO)_2]^{2-}$ Obtained from Single-crystal Structure.[67, 70]

Complexes	Fe_{1s}→Fe_{3d} Energy (eV)	δ (mm/s)	ΔE_Q (mm/s)	ν_{NO} (cm^{-1})[b]	ν_{CO} (cm^{-1})[b]	Fe–NO (Å)[c]	N–O (Å)[c]	Fe–N_{Pyr} (Å)[c]	Fe···Fe (Å)	Fe–C (Å)[c]	Ref.
1-PPh4	7113.6	0.10	0.35	1706, 1694	1846	1.65	1.18	-	2.60	1.94	[70]
2-K-crown	7113.5	0.27	1.23	1639, 1592	-	1.65	1.21	2.03	4.03	-	[67]
3-K-crown	7113.7	0.16	0.60	1699, 1684	1840	1.65	1.19	1.98	2.74	1.91	This work
4-K-crown	-	0.02	0.41	1709, 1654	-	1.64	1.17	-	-	-	[66]
A-Na-cryptand	-	0.08	0.69	1743, 1718 1693	1989 1968	1.69	1.18	-	2.84	1.78	This work
$[(NO)_2Fe(\mu\text{-}SPh)_2Fe(NO)_2]^{2-}$	7113.3	-	-	1644, 1604	-	1.65	1.21	-	3.61	-	[70]

[a]Zero-field Mössbauer spectra were measured at 80K. [b]in THF. [c]Average bond distances.

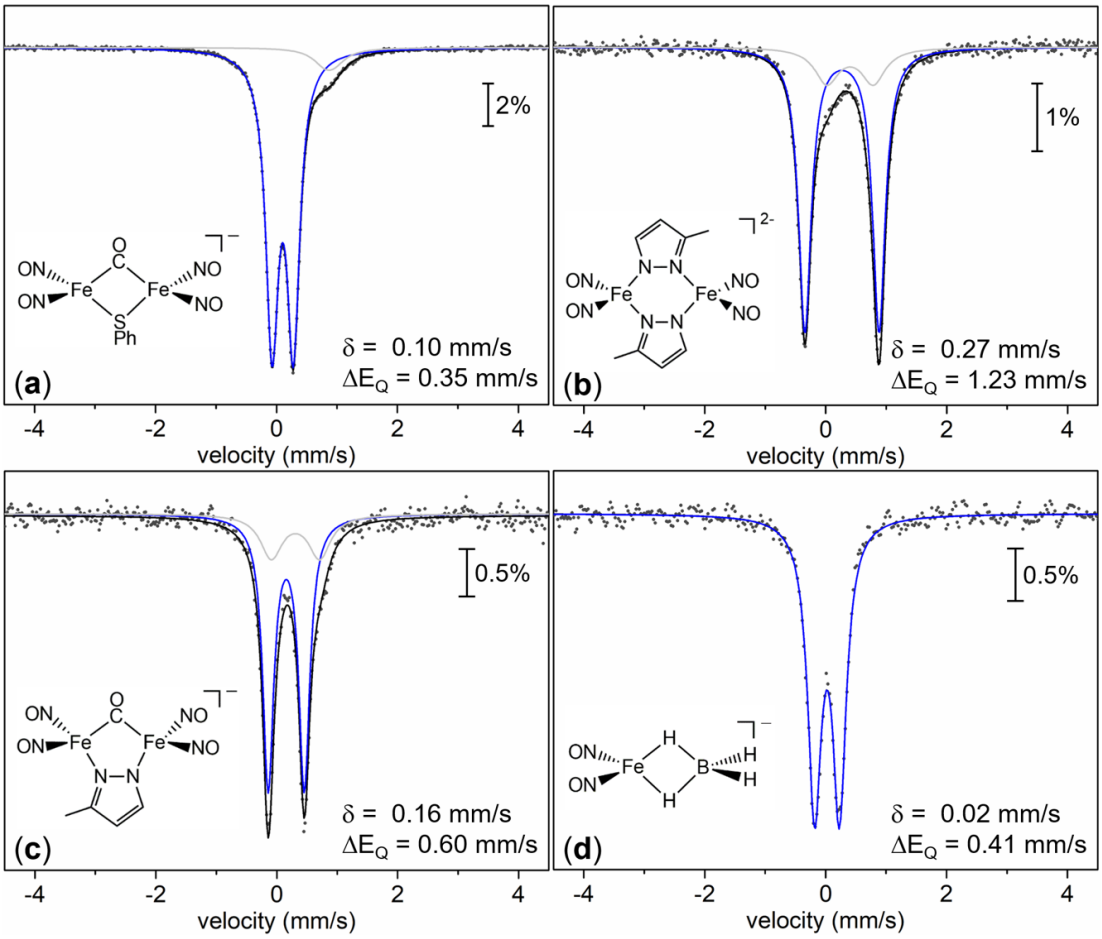

Figure 2. Zero-field Mössbauer spectra of DNICs (**a**) **1-PPh$_4$**, (**b**) **2-K-crown**, (**c**) **3-K-crown**, and (**d**) **4-Na-crown** collected at 80 K (dot). The blue lines are simulated spectra of these DNICs. Regarding the air-sensitive nature of DNICs **1-PPh$_4$**, **2-K-crown**, and **3-K-crown**, the gray lines are simulated spectra of minor impurities.

The electronic structure of DNIC **3-K-crown** was also explored by Mössbauer spectroscopy. Recently, a review on the Mössbauer spectroscopic study of DNICs explored a correlation between the isomer shift (δ) with the nature/type of supporting ligands to the [Fe(NO)$_2$] unit.[71] Among the structure-characterized DNICs, a higher Fe-L bond covalency between the [Fe(NO)$_2$] unit and supporting ligands (i.e. thiolate, carbene, CO) resulted in a smaller isomer shift (δ) of DNICs. Contrary to the isomer shift (δ) of 0.27 mm/s with a quadruple doublet (ΔE_Q) of 1.23 mm/s of DNIC **2-K-crown**, incorporation of π-acceptor CO bridging ligand in DNIC **3-K-crown** results in

a lower isomer shift (δ) of 0.16 mm/s with a quadruple doublet (ΔE_Q) of 0.60 mm/s (Figure 2 and Table 1).[71] Moreover, an isomer shift (δ) of 0.10 mm/s with a quadruple doublet (ΔE_Q) of 0.35 mm/s in DNIC **1-PPh$_4$** unraveled a covalent bonding interaction between the diamagnetic $\{Fe(NO)_2\}^{10}$-$\{Fe(NO)_2\}^{10}$ core and bridging $[SPh]^-$/CO ligands,[70, 74] which may rationalize the stability of [Fe(μ-CO)(μ-SPh)Fe] unit described below. Of interest, $\{Fe(NO)_2\}^{10}$ DNIC [Na-18-crown-6-ether][$(NO)_2Fe(\eta^2\text{-}BH_4)$] (**4-Na-crown**) exhibits an isomer shift (δ) of 0.02 mm/s with a quadruple doublet (ΔE_Q) of 0.41 mm/s.

Single-crystal X-ray diffraction study of DNIC **3-K-crown** provided direct insight into the geometric structure of dinuclear $\{Fe(NO)_2\}^{10}$ centers bridged by CO and 3-methylpyrazolate ligands (Figures 1b and S4). As shown in Table 1, average Fe–NO and N–O bond distances of 1.65 Å and 1.19 Å observed in DNIC **3-K-crown** are consistent with reported $\{Fe(NO)_2\}^{10}$ DNICs.[66] On the other hand, the average Fe-N_{pyr} bond distance of 1.98 Å observed in DNIC **3-K-crown** is slightly shorter than that of 2.03 Å in DNIC **2-K-crown**,[67] which echoed the π-acceptor effect of bridging CO ligand revealed by Fe K-edge XAS, ^{1}H NMR, and Mössbauer spectroscopy described above. Of importance, replacement of bridging phenylthiolate ligand in DNIC **1-PPh$_4$** by bridging 3-methylpyrazolate ligand in DNIC **3-K-crown** resulted in an elongation of Fe···Fe distance from 2.60 Å in the four-membered ring [Fe(μ-CO)(μ-SPh)Fe] to 2.74 Å in the five-membered ring [Fe(μ-CO)(μ-^{Me}Pyr)Fe]. Moreover, the Fe···Fe distance in the six-membered ring [Fe(μ-^{Me}Pyr)$_2$Fe] of DNIC **2-K-crown** elongated to 4.03 Å upon substitution of the bridging CO ligand in DNIC **3-K-crown** by another 3-methylpyrazole ligand. As opposed to the dihedral angle between two [$Fe(NO)_2$] planes of 180.0° featured by both DNICs **2-K-crown** and $[(NO)_2Fe(\mu\text{-}SPh)_2Fe(NO)_2]^{2-}$,

replacement with bridging CO ligand in DNICs **1-PPh4** and **3-K-crown** resulted in bent dihedral angles of 161.7° and 145.8°, respectively.[70] Based on the spectroscopic and crystallographic study, electron-deficient and structure-distorted [Fe(μ-CO)(μ-^{Me}Pyr)Fe] unit in DNIC **3-K-crown** was further explored for activation of dimethylamine borane (DMAB) regarding its potential electrophilic nature and prospective dissociation upon reaction with nucleophilic DMAB.

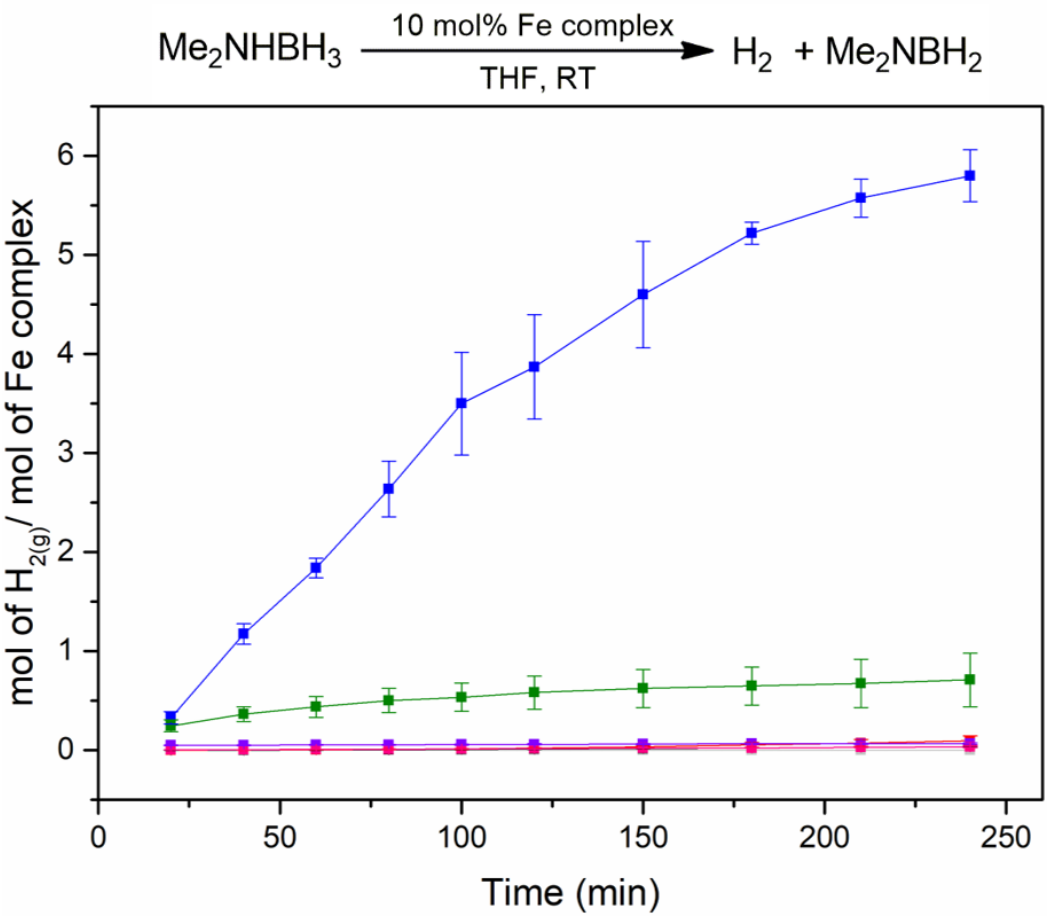

Figure 3. Evolution of $H_{2(g)}$ from reaction of DMAB without (gray) or with 10 mol% of DNICs **1-PPh4** (red), **2-K-crown** (black), **3-K-crown** (blue), **4-Na-crown** (purple), $Fe_2(CO)_9$ (green), and $[CpFe(CO)_2]_2$ (pink), respectively.

Investigation of DNIC 3-K-crown as a Pre-catalyst for Catalytic Dehydrogenation of DMAB via Formation of an Iron-Hydride Intermediate A. DNICs investigated for potential activation and catalytic dehydrogenation of DMAB in this study are shown in Chart 1b-1c. As shown in Figures 3 and S5a, formation of $H_{2(g)}$ from the THF solution of DMAB in the absence or presence of 10 mol% of Fe-CO complexes $[CpFe(CO)_2]_2$ and $Fe_2(CO)_9$, $\{Fe(NO)_2\}^{10}$-$\{Fe(NO)_2\}^{10}$ DNICs **1-PPh$_4$** and **2-K-crown**, and $\{Fe(NO)_2\}^{10}$ DNIC **4-Na-crown** is negligible. In contrast, addition of 10 mol% of DNIC **3-K-crown** into the THF solution of DMAB initiated the evolution of $H_{2(g)}$ which was detected by GC (Figures 3 and S5b). $H_{2(g)}$ evolution deceased after 4 h and the quantification of generated $H_{2(g)}$ revealed a turnover number (TON) of 6.0±0.2 for the dehydrogenation of DMAB catalyzed by DNIC **3-K-crown**, which is much lower than the other efficient molecular Fe catalysts.[3-8, 41] Additionally, full conversion of DMAB into released $H_{2(g)}$ promoted by 20 mol% of DNIC **3-K-crown** was optimized to enable the identification of generated cationic $[BH_2NHMe_2]^+$ and other boron-based byproducts using ^{11}B NMR (see details in Figure S6).[48, 75] In comparison with Fe-CO complexes and DNIC **1-PPh$_4$**/**2-K-crown**/**4-Na-crown**, the distinctive reactivity of DNIC **3-K-crown** toward catalytic dehydrogenation of DMAB prompted the subsequent spectroscopic and reactivity study in the attempt to gain the insights into the catalytic mechanism.

As shown in Figures S7-S9, no changes in the IR spectra were observed upon reaction of DMAB with 10 mol% of DNICs **1-PPh$_4$**, **2-K-crown**, and **4-Na-crown**, respectively. This indicated the inert nature of these DNICs toward DMAB, which is consistent with the absence and/or minor evolution of $H_{2(g)}$ described above. After addition of DMAB into the THF solution of 10 mol% of DNIC **3-K-crown** for 1 h, in contrast, appearance of IR ν_{NO} stretching frequencies at 1663 and 1610 cm^{-1} indicates

the partial generation of DNIC $[(NO)_2Fe(N,N'\text{-}^{Me}PyrBH_2NMe_2)]^-$ (**5**, Scheme 3a and Figure 4a), which was further characterized by ^1H NMR and single-crystal X-ray diffraction (Figures S10-S11). After a reaction time of 4 h, the distinctive IR ν_{NO} absorption peaks at (1663, 1610) cm^{-1} and ^1H NMR signals at (7.36, 5.79) ppm of DNIC **5** were retained (Figures 4b-4c) while the evolution of $H_{2(g)}$ deceased. That is, DNIC **5** serves as an inactive byproduct generated during the catalytic dehydrogenation of DMAB promoted by DNIC **3-K-crown**.

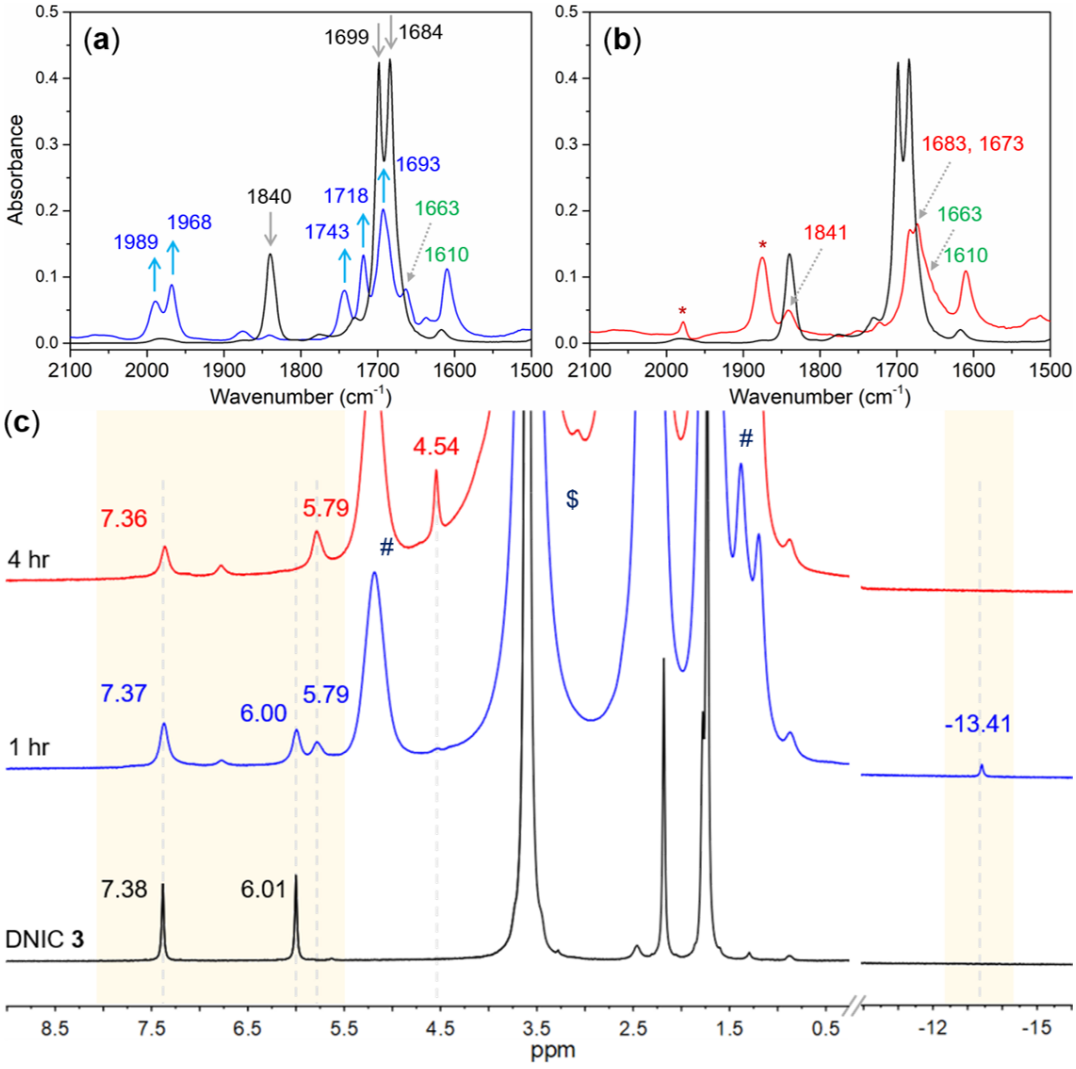

Figure 4. IR spectra of 10 mol% of DNIC **3-K-crown** before (black) and after its reaction with Me_2NHBH_3 for (**a**) 1 h (blue) and (**b**) 4 h (red) in THF. *: $[Fe(CO)_3(NO)]^-$. (**c**) ^1H NMR spectra of 20 mol% of DNIC **3-K-crown** before (black) and after its reaction with DMAB for 1 h (blue) and 4 h (red) in d_8-THF. (#: Me_2NHBH_3; $: 18-crown-6-ether).

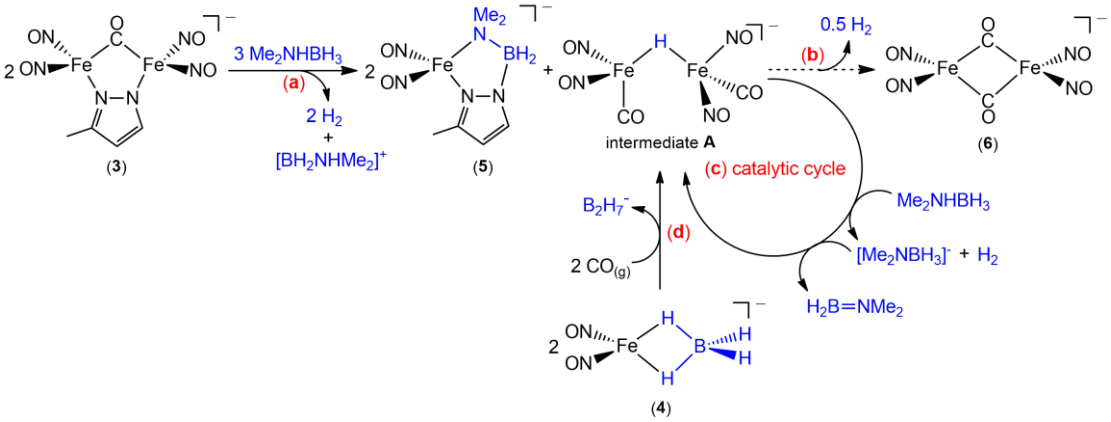

Scheme 3. Proposed mechanisms for substrate-gated transformation of pre-catalyst **3** into an iron-hydride intermediate **A** for catalytic dehydrogenation of dimethylamine borane.

In addition to the partial generation of DNIC **5** when DNIC **3-K-crown** reacted with 10 equiv. of DMAB in THF for 1 h, a shift of the IR ν_{CO} and ν_{NO} stretching frequencies from 1840 and (1699, 1684) cm^{-1} to (1989, 1968) and (1743, 1718, 1693) cm^{-1} reveals the parallel conversion of DNIC **3-K-crown** into an iron-hydride intermediate $[(NO)_2(CO)Fe(\mu\text{-}H)Fe(CO)(NO)_2]^-$ (**A**, Scheme 3a and Figure 4a),[76-78] which is further transformed into complexes $[(NO)_2Fe(\mu\text{-}CO)_2Fe(NO)_2]^-$ (**6**, yield 74.4%) and $[Fe(CO)_3(NO)]^-$ when $H_{2(g)}$ evolution stopped (Scheme 3b, Figures 4b and S12-S13). Notably, the absence of $H_{2(g)}$ evolution upon further addition of DMAB implicated that the iron-hydride species **A**, derived from reaction of pre-catalyst DNIC **3-K-crown** and DMAB, served as an intermediate during catalytic dehydrogenation of DMAB (Figure S14 and Scheme 3c). On the other hand, subsequent conversion of intermediate **A** into DNIC **6** resulted in the deactivation of catalytic process (Scheme 3b).

Reaction of the pre-catalyst DNIC **3-K-crown** and DMAB was also monitored by *in situ* ^1H NMR spectroscopy in the attempt to provide additional characterization of intermediate **A**. Upon addition of DMAB into the d_8-THF solution of 20 mol% of

DNIC **3-K-crown** at ambient temperature, formation of singlet ^{1}H NMR signals at (7.37, 5.79) and -13.41 ppm supported the conversion of DNIC **3-K-crown** into DNIC **5** and intermediate **A** in a 1:~0.4 molar ratio based on the intensity of the ^{1}H NMR signals (Scheme 3a and Figure 4c). After a reaction time of 4 h, the complete disappearance of the ^{1}H NMR signals of pre-catalyst DNIC **3-K-crown** and intermediate **A** accompanied by the formation of dissolved H_2, as evidenced by ^{1}H NMR signal at 4.54 ppm, highlighted that the iron-hydride species **A** was an intermediate generated during the catalytic dehydrogenation of DMAB.

Reactivity study of DNIC **3-K-crown** toward $H_{2(g)}$, NMe_2H, Et_3N-BH_3, and NMe_2H-BD_3, respectively, was performed in the attempt to dissect the mechanism for DMAB-mediated assembly of iron-hydride species **A**. As shown in Figure S15, DNIC **3-K-crown** displays inactive nature toward either $H_{2(g)}$ or NMe_2H. On the other hand, reaction of DNIC **3-K-crown** and 20 equiv. of triethylamine borane results in the absent evolution of $H_{2(g)}$ and the minor formation of IR ν_{CO} and ν_{NO} stretching frequencies at (1987, 1970) and (1741, 1716) cm^{-1} (Figure S16), which is comparable to the proposed iron-hydride species **A**. During the reaction of DNIC **3-K-crown** with NMe_2HBD_3, formation of a distinctive ^{2}D NMR signal at -13.41 ppm (Figure S17a) suggests that the hydridic nature of the B-H/B-D moiety in DMAB/NMe_2HBD_3 promotes the dissociation of [Fe(μ-CO)(μ-^{Me}Pyr)Fe] core for heterolytic cleavage of B-H/B-D bond and evolution of $H_{2(g)}$, which further results in the formation of DNIC **5** as an inactive byproduct (Scheme 3a). Moreover, subsequent activation of additional DMAB/NMe_2HBD_3 by the transient [(CO)Fe$(NO)_2$] cores facilitates heterolytic cleavage of B-H/B-D bond and assembly of iron-hydride species **A** accompanied by the formation of cationic $[BH_2NHMe_2]^{+}$.

Structural, Spectroscopic, and Computational Study of Intermediate A derived from Reaction of DNIC 4-Na-crown/4-Na-cryptand and $CO_{(g)}$. Inspired by the spectroscopic identification of DMAB-gated transformation of pre-catalyst DNIC **3-K-crown** into transient intermediate **A** during catalytic dehydrogenation of DMAB, efforts were further made on the development of alternative synthetic routes for the synthesis of intermediate **A**. When DNIC [Na-18-crown-6-ether][$(NO)_2Fe(\eta^2\text{-}BH_4)$] (**4-Na-crown**, or [Na-cryptand-222][$(NO)_2Fe(\eta^2\text{-}BH_4)$] (**4-Na-cryptand**)) was purged with $CO_{(g)}$ for 1 min, a shift of IR ν_{NO} stretching frequencies from (1708, 1654) to (1743, 1718, 1693) cm^{-1} as well as the appearance of IR ν_{CO} absorption peaks at (1989, 1968) cm^{-1} indicated the successful assembly of iron-hydride intermediate [Na-18-crown-6-ether][$(NO)_2(CO)Fe(\mu\text{-}H)Fe(CO)(NO)_2$] (**A-Na-crown**, or [Na-cryptand-222][$(NO)_2(CO)Fe(\mu\text{-}H)Fe(CO)(NO)_2$] (**A-Na-cryptand**), Scheme 3d and Figure 5a), which was substantiated by a sharp and singlet ^1H NMR signal at -13.41 ppm (Figures 5b and S18a). In addition to the IR ν_{CO} and ^1H NMR features, the ^{13}C NMR signal of terminal CO ligands in the diamagnetic intermediate **A-Na-cryptand** locates at 232.2 ppm (Figures 5b and S18b).[72-73] As shown in Figure 5c, $\{Fe(NO)_2\}^{10}$-$\{Fe(NO)_2\}^{10}$ intermediate **A-Na-cryptand** exhibits an isomer shift (δ) of 0.08 mm/s with a quadruple doublet (ΔE_Q) of 0.69 mm/s, which is comparable to $\{Fe(NO)_2\}^{10}$ DNIC **4-Na-crown** (Table 1).

In addition to the spectroscopic validation, catalytic generation of $H_{2(g)}$ from DMAB promoted by isolated **A-Na-crown** lended support to the assignment of iron-hydride species **A** as an intermediate generated during the catalytic dehydrogenation of DMAB by the pre-catalyst DNIC **3-K-crown** (Figure S19). Upon reaction of ^2H-labelled **A-Na-crown** with NMe_2HBD_3, evolution of HD was evidenced by the

indicative ^{1}H NMR signal at 4.51 ppm (triplet, $^{1}J_{HD}$ = 43 Hz, Figure S17b),[79] which supported the proposed mechanism for catalytic dehydrogenation of DMAB by intermediate **A** (Scheme 3c). Presumably, proton transfer from N-H fragment of DMAB to the bridging hydride in intermediate **A** is proposed to lead to the evolution of H_2, whereas the generated $[NMe_2BH_3]^-$ may serve as a hydride source to regenerate the iron-hydride species **A** accompanied by the formation of NMe_2BH_2 byproduct.

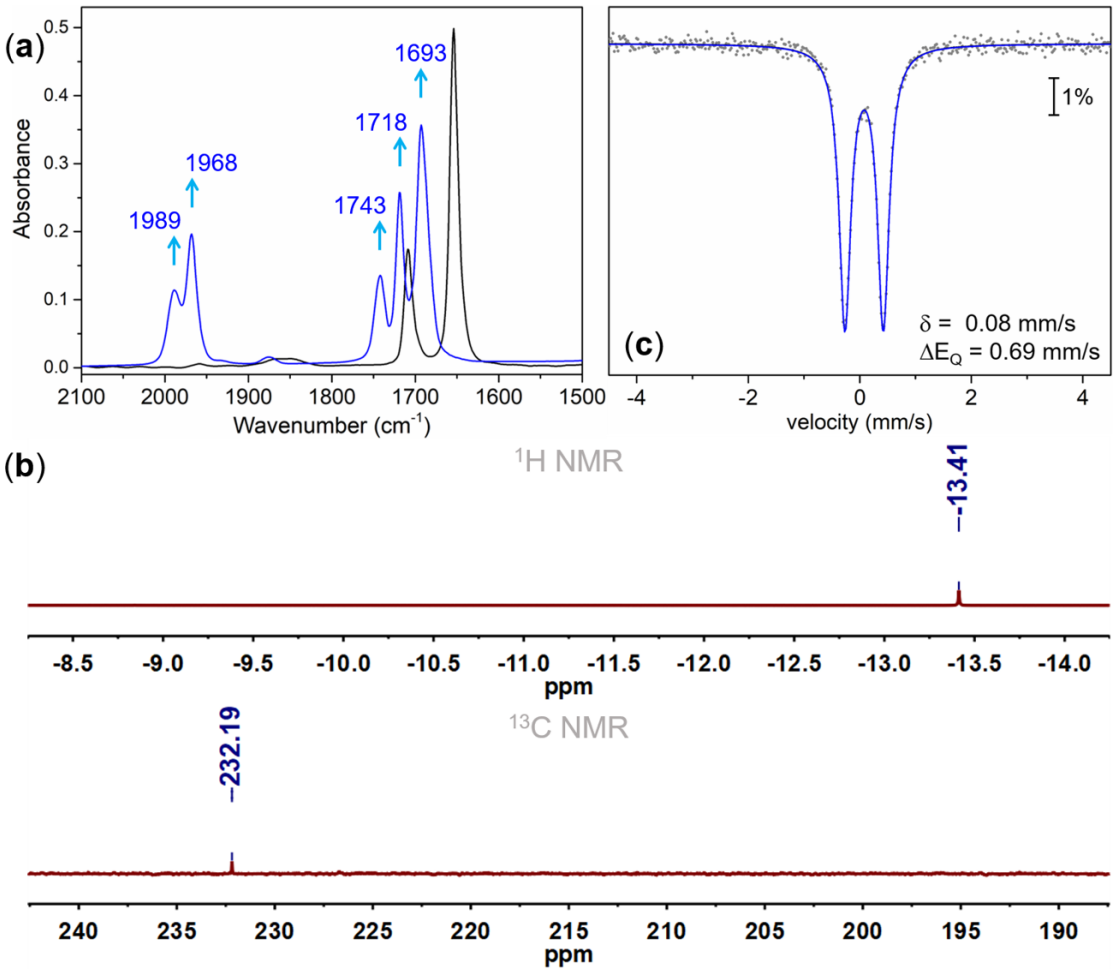

Figure 5. (**a**) IR spectra for DNIC **4-Na-cryptand** (black) and intermediate **A-Na-cryptand** (blue) in THF. (**b**) ^{1}H/^{13}C NMR spectra of intermediate **A-Na-cryptand** in d_8-THF. (**c**) Mössbauer spectrum of intermediate **A-Na-cryptand** collected at 80 K (dot). The blue line is simulated spectrum.

As shown in Figure 6, the single-crystal X-ray diffraction data provided direct support to intermediate **A-Na-cryptand** as an iron-hydride species. Similar to other $\{Fe(NO)_2\}^{10}$ DNICs, intermediate **A-Na-cryptand** featured average Fe–NO and N–O bond distances of 1.69 Å and 1.18 Å, respectively (Table 1).[66] In addition to the terminal CO ligand, an usual coordination of a bridging hydride ligand to each $[Fe(NO)_2]$ unit, with an average Fe-H bond distance of 1.58 Å, resulted in a tetrahedral geometry for both Fe centers. In comparison with other dinuclear $\{Fe(NO)_2\}^{10}$-$\{Fe(NO)_2\}^{10}$ DNICs, $\{Fe(NO)_2\}^{10}$ centers in intermediate **A-Na-cryptand** with one bridging hydride ligand featured an Fe–H–Fe bond angle of 128.0° and Fe···Fe distance of 2.84 Å.

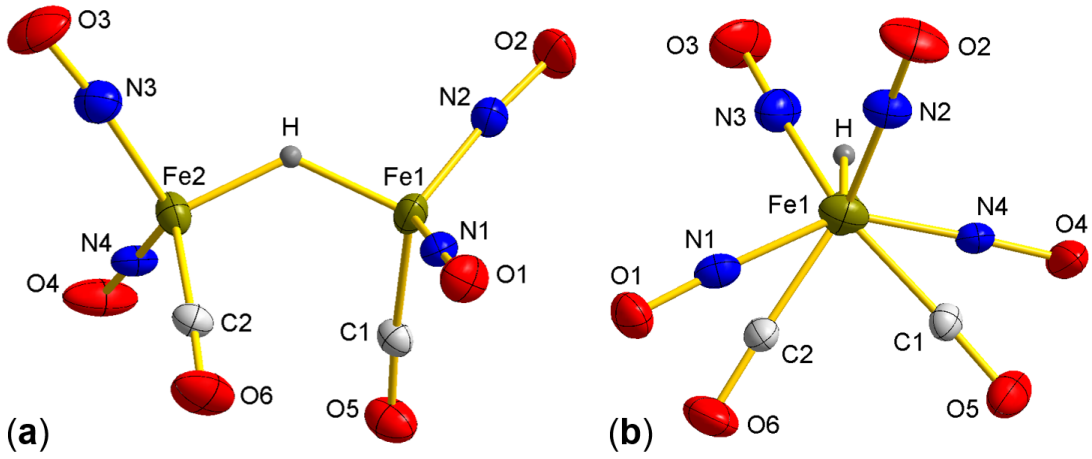

Figure 6. ORTEP drawing and labeling scheme for intermediate **A-Na-cryptand** with thermal ellipsoids drawn at 50% probability: (**a**) side view; (**b**) end view. [Na-cryptand-222]$^+$ countercation is omitted for clarity. Selected bond distances (Å) and angles (deg): Fe(1)···Fe(2) 2.8436(9); Fe(1)—H 1.591(50); Fe(2)—H 1.572(53); Fe(1)—N(1) 1.6826(28); Fe(1)—N(2) 1.6753(28); Fe(2)—N(3) 1.7205(49); Fe(2)—N(4) 1.6654(28); O(1)—N(1) 1.1836(38); O(2)—N(2) 1.1920(38); O(3)—N(3) 1.1643(59); O(4)—N(4) 1.1896(45); O(1)—N(1)—Fe(1) 175.6(2) (6); O(2)—N(2)—Fe(1) 173.5(2); O(3)—N(3)—Fe(2) 173.9(4); O(4)—N(4)—Fe(2) 175.5(2).

The iron-hydride species in intermediate **A-Na-cryptand** was additionally characterized using IR and nuclear resonance vibrational spectroscopy (NRVS) vibrational spectroscopies in combination with isotope-labelling experiments and computational methods for examination of the Fe-CO/NO/H bonding. Thereby, synchrotron-radiation based ^{57}Fe-NRVS provides a complete set of vibrations involving the iron nucleus and does not rely on any optical selection rules,[80] whereas the ^{57}Fe-partial vibrational density of states (PVDOS) spectra of ^{1}H-/^{2}H-labelled intermediate **A-Na-cryptand** are depicted in Figure 7. The ^{2}H-labelled compound **A-Na-cryptand** was prepared through reaction of ^{2}H-labelled DNIC **4-Na-cryptand** with $CO_{(g)}$ (Figure S20).

The DFT model of intermediate **A-Na-cryptand**, used for the assignment of solid-state IR and NRVS data, was originally based on the X-ray unit cell structure and is shown in Figure S21. The DFT-simulated ν_{NO} and ν_{CO} IR bands (Figure S22) repeated their experimentally observed pattern. Here, the bands at 1991 and 1963 cm^{-1} correspond to calculated symmetric and asymmetric stretching modes of the two CO ligands in **A-Na-cryptand**. The bands at 1743, 1717, and 1688 cm^{-1} correspond to the four NO stretching modes with different symmetries (see animations as part of the Supporting Information), where the flattened-top 1688 cm^{-1} band conceals two modes with similar energies. As detailed in Figure S22, the DFT calculations as well allow to quantify a concentration of the Hieber $[Fe(CO)_3(NO)]^-$ anion to approx. 10% relatively to **A-Na-cryptand** in the solid-state IR sample, matching the intensity of its minor feature appearing at 1877 cm^{-1}. Notably, the calculations reveal that bridging hydride motion admixes to the NO modes, which can be traced in a subtle red shift of the most prominent ν_{NO} band top (1688 to 1683 cm^{-1}) and its shoulder upon the μH-to-μD exchange. An essentially pure asymmetric Fe–μH(–Fe) stretch produces a low-intensity

DFT band at 1568 cm^{-1}, yet this feature lacks its counterpart in the experimental IR spectrum. The latter result goes in line with typically undetectably small signals of transition metal bridging hydrides by the IR technique.[81]

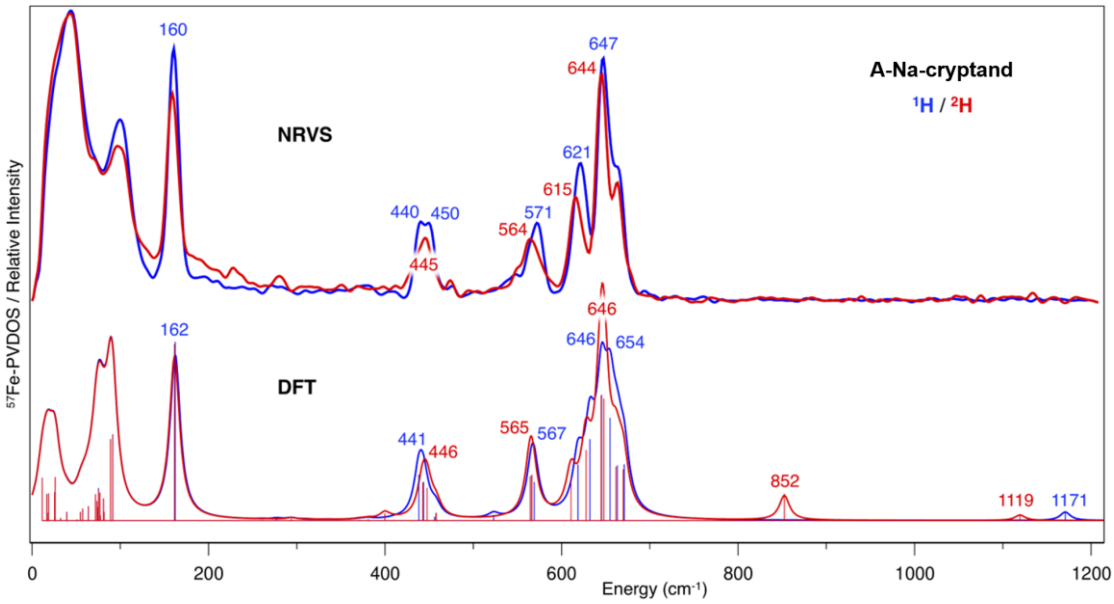

Figure 7. ^{57}Fe-PVDOS spectra of intermediate **A-Na-cryptand** (blue) overlaid with spectra of its ^{2}H-labelled isotopologue (red) from NRVS measurements (top) and DFT calculations (bottom). Sticks (bottom) highlight positions and intensities of the DFT-calculated normal modes. Selected band positions (see text) are labeled.

An attempt to reveal hydride bands in **A-Na-cryptand** was further undertaken using ^{57}Fe-NRVS spectroscopy that employed vibrational energy scans of up to 1200 cm^{-1} (Figure 7). The DFT calculations predicted several essentially pure Fe–hydride modes in the spectral region below 1200 cm^{-1}: (*i*) symmetric Fe–μH(–Fe) stretch at 1171 cm^{-1}, (*ii*) asymmetric Fe–μD(–Fe) stretch at 1119 cm^{-1}, and (*iii*) symmetric Fe–μD(–Fe) stretch at 852 cm^{-1} (see these and other NRVS-relevant normal modes animated as part of the Supporting Information). Although similar μH/μD modes with inherently low intensities were observed in diiron bridging hydride complexes using

^{57}Fe-NRVS previously,[82-84] present limitation to unenriched ^{57}Fe (2.12% natural abundance) samples of **A-Na-cryptand** precluded their definite resolution. Nevertheless, the high-intensity Fe–CO/NO bending and stretching modes in the 400–700 cm^{-1} region were computationally found to admix with the hydride wagging motion, typically leading to their red shifts within 10 cm^{-1} upon the μD-labeling. These isotope-dependent changes manifest in the bands at 571/564, 621/615, and 647/644 cm^{-1} for the μH/μD samples correspondingly, and in a μH-to-μD perturbation of a feature containing several Fe–CO/NO modes at approx. 445 cm^{-1} (Figure 7). Finally, a unique spectroscopic feature of **A-Na-cryptand** is a Fe–μH–Fe bending motion, producing a sharp band at 160 cm^{-1}.

NRVS spectra were additionally recorded for the ^{1}H- and ^{2}H-labelled samples of DNIC **4-Na-crown** (Figures S23 and S24). Within the experimental range of up to 1300 cm^{-1}, DFT predicts stand-alone low-intensity bands at 827 and 1002 cm^{-1} for the unlabeled and ^{2}H-lableled species, correspondingly. These bands are produced by hydride bends of the Fe-bound borontetrahydride (see normal modes animated as part of the Supporting Information). Similar to **A-Na-cryptand**, the NRVS scans of **4-Na-crown** used unenriched ^{57}Fe samples and could not reveal these weak spectral features. The isotope-dependent spectral perturbations are still observed in the 500–700 cm^{-1} region containing high-intensity Fe–NO modes, which range is typically for $\{Fe(NO)_2\}^{10}$ compounds.[85] A strong shift of approx. 30 cm^{-1} is predicted for the Fe–η^2BH_4/η^2BD_4 stretching mode, tentatively associated with features observed at 412/383 cm^{-1}.

Conclusion

In this study, synthesis and characterization of DNIC $[(NO)_2Fe(\mu\text{-}^{Me}Pyr)(\mu\text{-}CO)Fe(NO)_2]^-$ (**3**) as a pre-catalyst for dehydrogenation of DMAB via formation of an Fe-H intermediate $[(NO)_2(CO)Fe(\mu\text{-}H)Fe(CO)(NO)_2]^-$ (**A**) have led to the following results:

1. Through reaction of DNICs $Fe(CO)_2(NO)_2$ and **2-K-crown** in a 1:0.5 molar ratio, diamagnetic $\{Fe(NO)_2\}^{10}$-$\{Fe(NO)_2\}^{10}$ DNIC **3-K-crown** was successfully synthesized and characterized by IR, $^1H/^{13}C$ NMR, Fe K-edge XAS, Mössbauer, and single-crystal X-ray diffraction. As opposed to Fe-CO complexes $[CpFe(CO)_2]_2$ and $Fe_2(CO)_9$ as well as DNICs **1-PPh4**, **2-K-crown**, and **4-Na-crown**, this DNIC **3-K-crown** features catalytic reactivity toward dehydrogenation of DMAB with a turnover number (TON) of 6.0±0.2 and relies only on earth-abundant metals. Despite of the limited catalytic efficacy of DNIC **3-K-crown** for evolution of $H_{2(g)}$ from DMAB, continued investigations of DNICs featuring improved reactivity for catalytic dehydrogenation of amine boranes and hydrogenation of other substrates will be explored in the near future.

2. During the catalytic dehydrogenation of DMAB promoted by DNIC **3-K-crown**, the start and end of the $H_{2(g)}$ evolution is synchronized with the formation of intermediate **A** and its conversion into DNIC $[(NO)_2Fe(\mu\text{-}CO)_2Fe(NO)_2]^-$ (**6**), whereas a byproduct DNIC $[(NO)_2Fe(N,N'\text{-}^{Me}PyrBH_2NMe_2)]^-$ (**5**) remains observed through the catalytic process. That is, DNIC **3-K-crown** serves as a pre-catalyst for catalytic dehydrogenation of DMAB and evolution of $H_{2(g)}$ via a DMAB-gated assembly of intermediate **A**.

3. Reaction of DNIC **4-Na-crown**/**4-Na-cryptand** and $CO_{(g)}$ was discovered as an alternative synthetic route for preparation of isolated intermediate **A-Na-crown**/**A-Na-cryptand**, which exhibited consistent spectroscopic features and catalytic reactivity to the transient intermediate **A** derived from reaction of pre-catalyst DNIC **3-K-crown** and excess DMAB. Furthermore, single-crystal X-ray diffraction, IR, nuclear resonance vibrational spectroscopy (NRVS) and theoretical calculation supported the assignment of intermediate **A** as a dinuclear iron-hydride species $[(NO)_2(CO)Fe(\mu\text{-}H)Fe(CO)(NO)_2]^-$. In contrast to the stability of DNIC $[(NO)_2Fe(\eta^2\text{-}BH_4)]^-$ (**4**), binding of CO to the $\{Fe(NO)_2\}^{10}$ unit within DNIC **4** triggers the heterolytic cleavage of B-H bond of Fe-bound $[BH_4]^-$, which is followed by the assembly of Fe-H intermediate **A** accompanied by the release of $[B_2H_7]^-$ upon reaction with another DNIC **4**.

4. Based on the spectroscopic, crystallographic, and reactivity studies, the electron-deficient and structure-distorted nature of DNIC **3-K-crown**, presumably, enables DMAB-gated dissociation of $[Fe(\mu\text{-}CO)(\mu\text{-}^{Me}Pyr)Fe]$ core for activation of DMAB and evolution of $H_{2(g)}$, which further results in the formation of DNIC **5** as an inactive byproduct. On the other hand, subsequent activation of DMAB by the transient $[(CO)Fe(NO)_2]$ core facilitates heterolytic cleavage of B-H bond and assembly of Fe-H intermediate **A**, which is relevant to CO-induced conversion of DNIC **4** into isolated intermediate **A**. In contrast to DNIC **3-K-crown**, the electron-rich $[Fe(\mu\text{-}^{Me}Pyr)_2Fe]$ core in DNIC **2-K-crown** and covalent $[Fe(\mu\text{-}CO)(\mu\text{-}SPh)Fe]$ core in DNIC **1-PPh$_4$** preclude the dissociation of diiron core and formation of a coordination-unsaturated $[(L)Fe(NO)_2]$ core for activation of DMAB and evolution of $H_{2(g)}$.

Acknowledgments

We gratefully acknowledge the financial support from the National Science and Technology Council (Taiwan), Deutsche Forschungsgemeinschaft (DFG, AP242/5-1 & under Germany's Excellence Strategy-EXC-2033-Projektnummer 390677874 "RESOLV", Germany´s Excellence Strategy - EXC 2186 - 390919832 - "The Fuel Science Center" and Germany´s Excellence Strategy – EXC 2008 – 390540038 – UniSysCat), and the Fraunhofer Internal Programs (Attract 097-602175). We thank Ms. Pei-Lin Chen (National Tsing Hua University), Dr. Ting-Shen Kuo and Ms. Kai-Jieah Hsing (National Taiwan Normal University) for the single-crystal X-ray structural determinations; Ms. Hui-Chi Tan (National Tsing Hua University) for the NMR measurements. Parts of this research were carried out at PETRA III and SPring8. We would like to thank Dr. A. Jafari and Dr. H. Matsuura for assistance in using P01 and Bl09XU. Beamtime was allocated for proposals I-20210059, I-20211258 and 2020A1450. The National Synchrotron Radiation Research Center (Taiwan) is acknowledged for the support on XAS measurements.

Supporting Information Available: Supplementary figures and tables for additional experimental results including Fe K-edge XAS, IR, $^{1}H/^{11}B/^{13}C$ NMR, and ^{57}Fe-PVDOS spectra, evolution of $H_{2(g)}$ monitored by GC under different conditions, ORTEP drawing and labeling scheme for complexes **3-K-crown**/**5-K-crown**/**6-K-crown**, animated vibrational modes and cartesian coordinates of the DFT-optimized models of intermediate **A-Na-cryptand** and DNIC **4-Na-crown**, and crystal data and structure refinement for complexes **3-K-crown**/**5-K-crown**/**6-K-crown**/**A-Na-cryptand**. This material is available free of charge via the Internet at http://pubs.acs.org.

Reference

1. Stephens, F. H.; Pons, V.; Tom Baker, R., Ammonia-borane: the hydrogen source par excellence? *Dalton Trans.* **2007,** (25), 2613-2626.

2. Dorn, H.; Vejzovic, E.; Lough, A. J.; Manners, I., Rhodium-catalyzed dehydrocoupling of the sterically encumbered phosphine-borane adduct tBu$_2$PH.BH$_3$: synthesis of the linear dimers tBu$_2$PH.BH$_2$-tBu$_2$P.BH$_3$ and tBu$_2$PH.BH$_2$-tBu$_2$P.BH$_2$Cl. *Inorg. Chem.* **2001,** *40* (17), 4327-4331.
3. Rossin, A.; Peruzzini, M., Ammonia-Borane and Amine-Borane Dehydrogenation Mediated by Complex Metal Hydrides. *Chem. Rev.* **2016,** *116* (15), 8848-8872.
4. Han, D. L.; Anke, F.; Trose, M.; Beweries, T., Recent advances in transition metal catalysed dehydropolymerisation of amine boranes and phosphine boranes. *Coord. Chem. Rev.* **2019,** *380*, 260-286.
5. Johnson, H. C.; Hooper, T. N.; Weller, A. S., The Catalytic Dehydrocoupling of Amine–Boranes and Phosphine–Boranes. In *Synthesis and Application of Organoboron Compounds*, Fernández, E.; Whiting, A., Eds. Springer International Publishing: Cham, 2015; pp 153-220.
6. Colebatch, A. L.; Weller, A. S., Amine-Borane Dehydropolymerization: Challenges and Opportunities. *Chem. Eur. J.* **2019,** *25* (6), 1379-1390.
7. Hamilton, C. W.; Baker, R. T.; Staubitz, A.; Manners, I., B-N compounds for chemical hydrogen storage. *Chem. Soc. Rev.* **2009,** *38* (1), 279-93.
8. Alig, L.; Fritz, M.; Schneider, S., First-Row Transition Metal (De)Hydrogenation Catalysis Based On Functional Pincer Ligands. *Chem. Rev.* **2019,** *119* (4), 2681-2751.
9. Miranda, C. R.; Ceder, G., Ab initio investigation of ammonia-borane complexes for hydrogen storage. *J. Chem. Phys.* **2007,** *126* (18), 184703.
10. Davis, B. L.; Dixon, D. A.; Garner, E. B.; Gordon, J. C.; Matus, M. H.; Scott, B.; Stephens, F. H., Efficient regeneration of partially spent ammonia borane fuel. *Angew. Chem. Int. Ed.* **2009,** *48* (37), 6812-6816.
11. Sutton, A. D.; Burrell, A. K.; Dixon, D. A.; Garner, E. B., 3rd; Gordon, J. C.; Nakagawa, T.; Ott, K. C.; Robinson, J. P.; Vasiliu, M., Regeneration of ammonia borane spent fuel by direct reaction with hydrazine and liquid ammonia. *Science* **2011,** *331* (6023), 1426-9.
12. Yang, X.; Zhao, L.; Fox, T.; Wang, Z. X.; Berke, H., Transfer hydrogenation of imines with ammonia-borane: a concerted double-hydrogen-transfer reaction. *Angew. Chem. Int. Ed.* **2010,** *49* (11), 2058-2062.
13. Li, S.; Li, G.; Meng, W.; Du, H., A Frustrated Lewis Pair Catalyzed Asymmetric Transfer Hydrogenation of Imines Using Ammonia Borane. *J. Am. Chem. Soc.* **2016,** *138* (39), 12956-12962.
14. Jiang, Y.; Berke, H., Dehydrocoupling of dimethylamine-borane catalysed by rhenium complexes and its application in olefin transfer-hydrogenations. *Chem. Comm.* **2007,** (34), 3571-3.
15. Jiang, Y. F.; Blacque, O.; Fox, T.; Frech, C. M.; Berke, H., Development of Rhenium Catalysts for Amine Borane Dehydrocoupling and Transfer Hydrogenation of Olefins. *Organometallics* **2009,** *28* (18), 5493-5504.
16. Zhao, T. J.; Zhang, Y. N.; Wang, K. X.; Su, J.; Wei, X.; Li, X. H., General transfer hydrogenation by activating ammonia-borane over cobalt nanoparticles. *RSC Adv.* **2015,** *5* (124), 102736-102740.
17. Fang, M.-H.; Wu, S.-Y.; Chang, Y.-H.; Narwane, M.; Chen, B.-H.; Liu, W.-L.; Kurniawan, D.; Chiang, W.-H.; Lin, C.-H.; Chuang, Y.-C.; Hsu, I.-J.; Chen, H.-T.; Lu, T.-T., Mechanistic Insight into the Synergetic Interaction of Ammonia Borane and Water on ZIF-67-Derived Co@Porous Carbon for Controlled Generation of Dihydrogen. *ACS Appl. Mater. Interfaces* **2021,** *13* (40), 47465-47477.

18. Peng, C. Y.; Kang, L.; Cao, S.; Chen, Y.; Lin, Z. S.; Fu, W. F., Nanostructured Ni_2P as a Robust Catalyst for the Hydrolytic Dehydrogenation of Ammonia-Borane. *Angew. Chem.* **2015,** *54* (52), 15725-15729.
19. Li, Z.; He, T.; Matsumura, D.; Miao, S.; Wu, A. A.; Liu, L.; Wu, G.; Chen, P., Atomically Dispersed Pt on The Surface of Ni Particles: Synthesis and Catalytic Function in Hydrogen Generation from Aqueous Ammonia-Borane. *ACS Catal.* **2017,** *7* (10), 6762-6769.
20. Shimoi, M.; Nagai, S.-i.; Ichikawa, M.; Kawano, Y.; Katoh, K.; Uruichi, M.; Ogino, H., Coordination Compounds of Monoborane−Lewis Base Adducts: Syntheses and Structures of [M(CO)5(η1-BH3·L)] (M = Cr, Mo, W; L = NMe3, PMe3, PPh3). *J. Am. Chem. Soc.* **1999,** *121* (50), 11704-11712.
21. Kakizawa, T.; Kawano, Y.; Shimoi, M., Syntheses and Structures of Manganese Complexes of Borane−Lewis Base Adducts, [CpMn(CO)2(η1-BH3·L)] (L = NMe3, PMe3). *Organometallics* **2001,** *20* (15), 3211-3213.
22. Nako, A. E.; White, A. J. P.; Crimmin, M. R., Bis(σ-B–H) complexes of copper(i): precursors to a heterogeneous amine–borane dehydrogenation catalyst. *Dalton Trans.* **2015,** *44* (28), 12530-12534.
23. Chapman, A. M.; Haddow, M. F.; Wass, D. F., Frustrated Lewis Pairs beyond the Main Group: Cationic Zirconocene–Phosphinoaryloxide Complexes and Their Application in Catalytic Dehydrogenation of Amine Boranes. *J. Am. Chem. Soc.* **2011,** *133* (23), 8826-8829.
24. Kawano, Y.; Hashiva, M.; Shimoi, M., Syntheses and Reactivity of Cationic Borane−Ruthenium Complexes [(η5-C5R5)Ru(PMe3)2(η1-BH3·EMe3)][BArf4] (R = H, Me; E = N, P; BArf4 = [B{3,5-C6H3(CF3)2}4]). *Organometallics* **2006,** *25* (18), 4420-4426.
25. Adams, G. M.; Colebatch, A. L.; Skornia, J. T.; McKay, A. I.; Johnson, H. C.; Lloyd−Jones, G. C.; Macgregor, S. A.; Beattie, N. A.; Weller, A. S., Dehydropolymerization of $H_3B{\cdot}NMeH_2$ To Form Polyaminoboranes Using [Rh(Xantphos-alkyl)] Catalysts. *J. Am. Chem. Soc.* **2018,** *140* (4), 1481-1495.
26. Kumar, A.; Johnson, H. C.; Hooper, T. N.; Weller, A. S.; Algarra, A. G.; Macgregor, S. A., Multiple metal-bound oligomers from Ir-catalysed dehydropolymerisation of $H_3B{\cdot}NH_3$ as probed by experiment and computation. *Chem. Sci.* **2014,** *5* (6), 2546-2553.
27. Stennett, T. E.; Harder, S., s-Block amidoboranes: syntheses, structures, reactivity and applications. *Chem. Soc. Rev.* **2016,** *45* (4), 1112-1128.
28. Bellham, P.; Hill, M. S.; Kociok-Köhn, G.; Liptrot, D. J., Alkaline earth alkyl insertion chemistry of in situ generated aminoboranes. *Dalton Trans.* **2013,** *42* (3), 737-745.
29. Xu, P.; Xu, X., Dehydrogenation of (Di)amine–Boranes by Highly Active Scandocene Alkyl Catalysts. *Organometallics* **2019,** *38* (16), 3212-3217.
30. LaPierre, E. A.; Patrick, B. O.; Manners, I., Trivalent Titanocene Alkyls and Hydrides as Well-Defined, Highly Active, and Broad Scope Precatalysts for Dehydropolymerization of Amine-Boranes. *J. Am. Chem. Soc.* **2019,** *141* (51), 20009-20015.
31. Nugent, J. W.; García-Melchor, M.; Fout, A. R., Cobalt-Catalyzed Ammonia Borane Dehydrogenation: Mechanistic Insight and Isolation of a Cobalt Hydride-Amidoborane Complex. *Organometallics* **2020,** *39* (15), 2917-2927.
32. Erickson, K. A.; Stelmach, J. P. W.; Mucha, N. T.; Waterman, R., Zirconium-Catalyzed Amine Borane Dehydrocoupling and Transfer Hydrogenation. *Organometallics* **2015,** *34* (19), 4693-4699.

33. Cui, P.; Spaniol, T. P.; Maron, L.; Okuda, J., Dehydrogenation of Amine□Borane Me2NH·BH3 Catalyzed by a Lanthanum□Hydride Complex. *Chem. Eur. J.* **2013,** *19* (40), 13437-13444.
34. Chaplin, A. B.; Weller, A. S., B□H Activation at a Rhodium(I) Center: Isolation of a Bimetallic Complex Relevant to the Transition-Metal-Catalyzed Dehydrocoupling of Amine–Boranes. *Angew. Chem Int. Ed.* **2010,** *49* (3), 581-584.
35. Helten, H.; Dutta, B.; Vance, J. R.; Sloan, M. E.; Haddow, M. F.; Sproules, S.; Collison, D.; Whittell, G. R.; Lloyd-Jones, G. C.; Manners, I., Paramagnetic Titanium(III) and Zirconium(III) Metallocene Complexes as Precatalysts for the Dehydrocoupling/Dehydrogenation of Amine–Boranes. *Angew. Chem. Int. Ed.* **2013,** *52* (1), 437-440.
36. Forster, T. D.; Tuononen, H. M.; Parvez, M.; Roesler, R., Characterization of β-B-Agostic Isomers in Zirconocene Amidoborane Complexes. *J. Am. Chem. Soc.* **2009,** *131* (19), 6689-6691.
37. Kwan, E. H.; Ogawa, H.; Yamashita, M., A Highly Active PBP–Iridium Catalyst for the Dehydrogenation of Dimethylamine–Borane: Catalytic Performance and Mechanism. *ChemCatChem* **2017,** *9* (13), 2457-2462.
38. Buss, J. A.; Edouard, G. A.; Cheng, C.; Shi, J.; Agapie, T., Molybdenum Catalyzed Ammonia Borane Dehydrogenation: Oxidation State Specific Mechanisms. *J. Am. Chem. Soc.* **2014,** *136* (32), 11272-11275.
39. Todisco, S.; Luconi, L.; Giambastiani, G.; Rossin, A.; Peruzzini, M.; Golub, I. E.; Filippov, O. A.; Belkova, N. V.; Shubina, E. S., Ammonia Borane Dehydrogenation Catalyzed by (κ4-EP3)Co(H) [EP3 = E(CH2CH2PPh2)3; E = N, P] and H2 Evolution from Their Interaction with NH Acids. *Inorg. Chem.* **2017,** *56* (8), 4296-4307.
40. Baker, R. T.; Gordon, J. C.; Hamilton, C. W.; Henson, N. J.; Lin, P. H.; Maguire, S.; Murugesu, M.; Scott, B. L.; Smythe, N. C., Iron complex-catalyzed ammonia-borane dehydrogenation. A potential route toward B-N-containing polymer motifs using earth-abundant metal catalysts. *J. Am. Chem. Soc.* **2012,** *134* (12), 5598-609.
41. Gluer, A.; Forster, M.; Celinski, V. R.; auf der Gunne, J. S.; Holthausen, M. C.; Schneider, S., Highly Active Iron Catalyst for Ammonia Borane Dehydrocoupling at Room Temperature. *ACS Catal.* **2015,** *5* (12), 7214-7217.
42. Anke, F.; Han, D.; Klahn, M.; Spannenberg, A.; Beweries, T., Formation of high-molecular weight polyaminoborane by Fe hydride catalysed dehydrocoupling of methylamine borane. *Dalton Trans.* **2017,** *46* (21), 6843-6847.
43. Elsby, M. R.; Ghostine, K.; Das, U. K.; Gabidullin, B. M.; Baker, R. T., Iron-SNS and -CNS Complexes: Selective C-aryl-S Bond Cleavage and Amine-Borane Dehydrogenation Catalysis. *Organometallics* **2019,** *38* (19), 3844-3851.
44. Anke, F.; Boye, S.; Spannenberg, A.; Lederer, A.; Heller, D.; Beweries, T., Dehydropolymerisation of Methylamine Borane and an N-Substituted Primary Amine Borane Using a PNP Fe Catalyst. *Chem. Eur. J.* **2020,** *26* (35), 7889-7899.
45. Knitsch, R.; Han, D. L.; Anke, F.; Ibing, L.; Jiao, H. J.; Hansen, M. R.; Beweries, T., Fe(II) Hydride Complexes for the Homogeneous Dehydrocoupling of Hydrazine Borane: Catalytic Mechanism via DFT Calculations and Detailed Spectroscopic Characterization. *Organometallics* **2019,** *38* (14), 2714-2723.
46. Das, U. K.; Daifuku, S. L.; Iannuzzi, T. E.; Gorelsky, S. I.; Korobkov, I.; Gabidullin, B.; Neidig, M. L.; Baker, R. T., Iron(II) Complexes of a Hemilabile SNS Amido. Ligand: Synthesis, Characterization, and Reactivity. *Inorg. Chem.* **2017,** *56* (22), 13766-13776.

47. Roselló-Merino, M.; López-Serrano, J.; Conejero, S., Dehydrocoupling reactions of dimethylamine-borane by Pt(II) complexes: a new mechanism involving deprotonation of boronium cations. *J. Am. Chem. Soc.* **2013,** *135* (30), 10910-10913.
48. Spearing-Ewyn, E. A. K.; Beattie, N. A.; Colebatch, A. L.; Martinez-Martinez, A. J.; Docker, A.; Boyd, T. M.; Baillie, G.; Reed, R.; Macgregor, S. A.; Weller, A. S., The role of neutral Rh(PONOP)H, free NMe_2H, boronium and ammonium salts in the dehydrocoupling of dimethylamine-borane using the cationic pincer $[Rh(PONOP)(\eta^2\text{-}H_2)]^+$ catalyst. *Dalton Trans.* **2019,** *48* (39), 14724-14736.
49. Vance, J. R.; Robertson, A. P.; Lee, K.; Manners, I., Photoactivated, iron-catalyzed dehydrocoupling of amine-borane adducts: formation of boron-nitrogen oligomers and polymers. *Chem. Eur. J.* **2011,** *17* (15), 4099-4103.
50. Coles, N. T.; Webster, R. L., Iron Catalyzed Dehydrocoupling of Amine- and Phosphine-Boranes. *Isr. J. Chem.* **2017,** *57* (12), 1070-1081.
51. Shimbayashi, T.; Fujita, K., Metal-catalyzed hydrogenation and dehydrogenation reactions for efficient hydrogen storage. *Tetrahedron* **2020,** *76* (11).
52. Vance, J. R.; Schafer, A.; Robertson, A. P.; Lee, K.; Turner, J.; Whittell, G. R.; Manners, I., Iron-catalyzed dehydrocoupling/dehydrogenation of amine-boranes. *J. Am. Chem. Soc.* **2014,** *136* (8), 3048-3064.
53. Lunsford, A. M.; Blank, J. H.; Moncho, S.; Haas, S. C.; Muhammad, S.; Brothers, E. N.; Darensbourg, M. Y.; Bengali, A. A., Catalysis and Mechanism of H2 Release from Amine-Boranes by Diiron Complexes. *Inorg. Chem.* **2016,** *55* (2), 964-973.
54. Hsieh, C.-H.; Ding, S.; Erdem, Ö. F.; Crouthers, D. J.; Liu, T.; McCrory, C. C.; Lubitz, W.; Popescu, C. V.; Reibenspies, J. H.; Hall, M. B.; Darensbourg, M. Y., Redox active iron nitrosyl units in proton reduction electrocatalysis. *Nat. Comm.* **2014,** *5*, 3684 doi: 10.1038/ncomms4684.
55. Ghosh, P.; Ding, S. D.; Chupik, R. B.; Quiroz, M.; Hsieh, C. H.; Bhuvanesh, N.; Hall, M. B.; Darensbourg, M. Y., A matrix of heterobimetallic complexes for interrogation of hydrogen evolution reaction electrocatalysts. *Chem. Sci.* **2017,** *8* (12), 8291-8300.
56. Ding, S.; Ghosh, P.; Darensbourg, M. Y.; Hall, M. B., Interplay of hemilability and redox activity in models of hydrogenase active sites. *Proc. Natl. Acad. Sci. U.S.A.* **2017,** *114* (46), E9775-E9782.
57. Chiou, T.-W.; Lu, T.-T.; Wu, Y.-H.; Yu, Y.-J.; Chu, L.-K.; Liaw, W.-F., Development of a Dinitrosyl Iron Complex Molecular Catalyst into a Hydrogen Evolution Cathode. *Angew. Chem. Int. Ed.* **2015,** *54*, 14824 –14829.
58. Nhut, G. T.; Kalyvas, H.; Skodje, K. M.; Hayashi, T.; Moenne-Loccoz, P.; Callan, P. E.; Shearer, J.; Kirschenbaum, L. J.; Kim, E., Phenol Nitration Induced by an $\{Fe(NO)_2\}^{10}$ Dinitrosyl Iron Complex. *J. Am. Chem. Soc.* **2011,** *133* (5), 1184-1187.
59. Lu, S.; Chiou, T.-W.; Li, W.-L.; Wang, C.-C.; Wang, Y.-M.; Lee, W.-Z.; Lu, T.-T.; Liaw, W.-F., Dinitrosyliron Complex $[(PMDTA)Fe(NO)_2]$: Intermediate for Nitric Oxide Monooxygenation Activity in Nonheme Iron Complex. *Inorg. Chem.* **2020,** *59*, 8308-8319.
60. Wu, W.-Y.; Hsu, C.-N.; Hsieh, C.-H.; Chiou, T.-W.; Tsai, M.-L.; Chiang, M.-H.; Liaw, W.-F., NO-to-$[N_2O_2]^{2-}$-to-N_2O Conversion Triggered by $\{Fe(NO)_2\}^{10}$-$\{Fe(NO)_2\}^9$ Dinuclear Dinitrosyl Iron Complex. *Inorg. Chem.* **2019,** *58* (15), 9586-9591.
61. Wu, W. Y.; Tsai, M. L.; Lai, Y. A.; Hsieh, C. H.; Liaw, W. F., NO Reduction to N2O Triggered by a Dinuclear Dinitrosyl Iron Complex via the Associated Pathways of Hyponitrite Formation and NO Disproportionation. *Inorg. Chem.* **2021**, ASAP.

62. Bar, A. K.; Heras Ojea, M. J.; Tang, J.; Layfield, R. A., Coupling of Nitric Oxide and Release of Nitrous Oxide from Rare-Earth-Dinitrosyliron Complexes. *J. Am. Chem. Soc.* **2020,** *142* (9), 4104-4107.
63. Tsai, F.-T.; Kuo, T.-S.; Liaw, W.-F., Dinitrosyl iron complexes (DNICs) bearing O-bound nitrito ligand: reversible transformation between the six-coordinate $\{Fe(NO)_2\}^9$ $[(1\text{-MeIm})_2(\eta^2\text{-ONO})Fe(NO)_2]$ (g = 2.013) and four-coordinate $\{Fe(NO)_2\}^9$ [(1-MeIm)(ONO)$Fe(NO)_2$] (g = 2.03). *J. Am. Chem. Soc.* **2009,** *131* (10), 3426-3427.
64. Tsai, F.-T.; Chen, P.-L.; Liaw, W.-F., Roles of the distinct electronic structures of the $\{Fe(NO)_2\}^9$ and $\{Fe(NO)_2\}^{10}$ dinitrosyliron complexes in modulating nitrite binding modes and nitrite activation pathways. *J. Am. Chem. Soc.* **2010,** *132* (14), 5290-5299.
65. Tsai, F.-T.; Lee, Y.-C.; Chiang, M.-H.; Liaw, W.-F., Nitrate-to-Nitrite-to-Nitric Oxide Conversion Modulated by Nitrate-Containing $\{Fe(NO)_2\}^9$ Dinitrosyl Iron Complex (DNIC). *Inorg. Chem.* **2013,** *52* (1), 464-473.
66. Huang, H.-C.; Ching, W.-M.; Tseng, Y.-T.; Chen, C.-H.; Lu, T.-T., Transformation of the hydride-containing dinitrosyl iron complex $[(NO)_2Fe(\eta^2\text{-}BH_4)]^-$ into $[(NO)_2Fe(\eta^3\text{-}HCS_2)]^-$ via reaction with CS_2. *Dalton Trans.* **2019,** *48*, 5897-5902.
67. Tseng, Y.-T.; Ching, W.-M.; Liaw, W.-F.; Lu, T.-T., Dinitrosyl Iron Complex [K-18-crown-6-ether][$(NO)_2Fe(^{Me}PyrCO_2)$]: Intermediate for Capture and Reduction of Carbon Dioxide. *Angew. Chem. Int. Ed.* **2020,** *59*, 11819-11823.
68. Scheidt, W. R.; Durbin, S. M.; Sage, J. T., Nuclear resonance vibrational spectroscopy--NRVS. *J. Inorg. Biochem.* **2005,** *99* (1), 60-71.
69. Cramer, S. P., Nuclear Resonaynce Vibrational Spectroscopy. In *X-Ray Spectroscopy with Synchrotron Radiation: Fundamentals and Applications*, Springer International Publishing: Cham, 2020; pp 257-278.
70. Lo, F.-C.; Li, Y.-W.; Hsu, I.-J.; Chen, C.-H.; Liaw, W.-F., Insight into the reactivity and electronic structure of dinuclear dinitrosyl iron complexes. *Inorg. Chem.* **2014,** *53* (20), 10881-10892.
71. Tung, C.-Y.; Tseng, Y.-T.; Lu, T.-T.; Liaw, W.-F., Insight into the Electronic Structure of Biomimetic Dinitrosyliron Complexes (DNICs): Toward the Syntheses of Amido-Bridging Dinuclear DNICs. *Inorg. Chem.* **2021,** *60* (21), 15846-15873.
72. Harris, D. C.; Rosenberg, E.; Roberts, J. D., Carbon-13 nuclear magnetic resonance spectra and mechanism of bridge–terminal carbonyl exchange in di-μ-carbonyl-bis[carbonyl(η-cyclopentadienyl)iron](Fe–Fe)[$\{(\eta\text{-}C_5H_5)Fe(CO)_2\}_2$]; *cd*-di-μ-carbonyl-*f*-carbonyl-*ae*-di(η-cyclopentadienyl)-*b*-(triethyl -phosphite)di-iron(Fe–Fe)[$(\eta\text{-}C_5H_5)_2Fe_2(CO)_3P(OEt)_3$], and some related complexes. *Dalton Trans.* **1974,** (22), 2398-2403.
73. Alvarez, M. A.; García, M. E.; González, R.; Ramos, A.; Ruiz, M. A., Synthesis and Decarbonylation Reactions of Diiron Cyclopentadienyl Complexes with Bent-Phosphinidene Bridges. *Organometallics* **2011,** *30* (5), 1102-1115.
74. Lu, T.-T.; Lai, S.-H.; Li, Y.-W.; Hsu, I.-J.; Jang, L.-Y.; Lee, J.-F.; Chen, I.-C.; Liaw, W.-F., Discrimination of mononuclear and dinuclear dinitrosyl iron complexes (DNICs) by S K-edge X-ray absorption spectroscopy: insight into the electronic structure and reactivity of DNICs. *Inorg. Chem.* **2011,** *50* (12), 5396-5406.
75. Rosello-Merino, M.; Lopez-Serrano, J.; Conejero, S., Dehydrocoupling reactions of dimethylamine-borane by Pt(II) complexes: a new mechanism involving deprotonation of boronium cations. *J. Am. Chem. Soc.* **2013,** *135* (30), 10910-3.
76. Laws, D. R.; Bullock, R. M.; Lee, R.; Huang, K. W.; Geiger, W. E., Comparison of the One-Electron Oxidations of CO-Bridged vs Unbridged Bimetallic Complexes:

Electron-Transfer Chemistry of $Os_2Cp_2(CO)_4$ and $Os_2Cp^*_2(\mu\text{-}CO)_2(CO)_2$ (Cp = η^5-C_5H_5, Cp* = η^5-C_5Me_5). *Organometallics* **2014,** *33* (18), 4716-4728.
77. Zhang, J.; Huang, K. W.; Szalda, D. J.; Bullock, R. M., Efficient synthesis of the Os-Os dimers $[CP(CO)_2Os]_2$, $[Cp^*(CO)_2Os]_2$, and $[(^iPr_4C_5H))(CO)_2Os]_2$ and computational studies on the relative stabilities of their geometrical isomers. *Organometallics* **2006,** *25* (9), 2209-2215.
78. Iffland, L.; Khedkar, A.; Petuker, A.; Lieb, M.; Wittkamp, F.; van Gastel, M.; Roemelt, M.; Apfel, U. P., Solvent-Controlled CO_2 Reduction by a Triphos-Iron Hydride Complex. *Organometallics* **2019,** *38* (2), 289-299.
79. Bodach, A.; Nothling, N.; Felderhoff, M., Activation of Molecular Hydrogen by Inter- and Intramolecular Al-N Lewis Pairs. *Eur. J. Inorg. Chem.* **2021,** *2021* (13), 1240-1243.
80. Lauterbach, L.; Gee, L. B.; Pelmenschikov, V.; Jenney, F. E.; Kamali, S.; Yoda, Y.; Adams, M. W.; Cramer, S. P., Characterization of the [3Fe-4S](0/1+) cluster from the D14C variant of Pyrococcus furiosus ferredoxin via combined NRVS and DFT analyses. *Dalton Trans.* **2016,** *45* (17), 7215-9.
81. Kaesz, H. D.; Saillant, R. B., Hydride complexes of the transition metals. *Chem. Rev.* **1972,** *72* (3), 231-281.
82. Gee, L. B.; Pelmenschikov, V.; Wang, H.; Mishra, N.; Liu, Y. C.; Yoda, Y.; Tamasaku, K.; Chiang, M. H.; Cramer, S. P., Vibrational characterization of a diiron bridging hydride complex - a model for hydrogen catalysis. *Chem. Sci.* **2020,** *11* (21), 5487-5493.
83. Pelmenschikov, V.; Gee, L. B.; Wang, H.; MacLeod, K. C.; McWilliams, S. F.; Skubi, K. L.; Cramer, S. P.; Holland, P. L., High-Frequency Fe-H Vibrations in a Bridging Hydride Complex Characterized by NRVS and DFT. *Angew. Chem. Int. Ed.* **2018,** *57* (30), 9367-9371.
84. Carlson, M. R.; Gray, D. L.; Richers, C. P.; Wang, W.; Zhao, P. H.; Rauchfuss, T. B.; Pelmenschikov, V.; Pham, C. C.; Gee, L. B.; Wang, H.; Cramer, S. P., Sterically Stabilized Terminal Hydride of a Diiron Dithiolate. *Inorg. Chem.* **2018,** *57* (4), 1988-2001.
85. Speelman, A. L.; Zhang, B.; Silakovi, A.; Skodje, K. M.; Alp, E. E.; Zhao, J.; Hu, M. Y.; Kim, E.; Krebs, C.; Lehnert, N., Unusual Synthetic Pathway for an $\{Fe(NO)_2\}^9$ Dinitrosyl Iron Complex (DNIC) and Insight into DNIC Electronic Structure via Nuclear Resonance Vibrational Spectroscopy. *Inorg. Chem.* **2016,** *55* (11), 5485-5501.

TOC

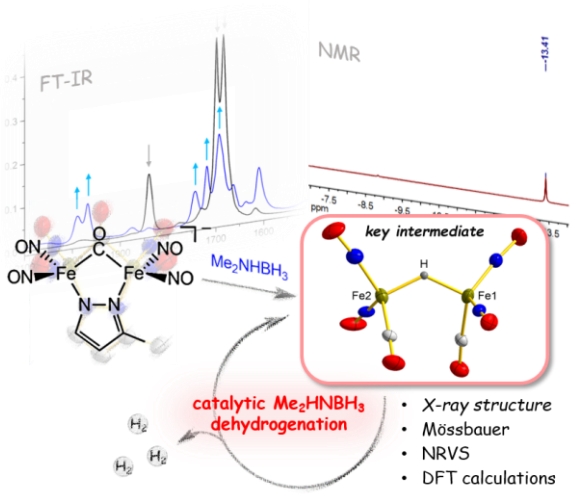

Through substrate-gated activation of a pre-catalyst $[(NO)_2Fe(\mu\text{-}^{Me}Pyr)(\mu\text{-}CO)Fe(NO)_2]^-$, an iron-hydride species $[(NO)_2(CO)Fe(\mu\text{-}H)Fe(CO)(NO)_2]^-$, as evidenced by different spectroscopic methods and DFT calculations, was identified as the active intermediate for catalytic dehydrogenation of dimethylamine borane and generation of $H_{2(g)}$.